

A Lensing Survey of X-ray Luminous Galaxy Clusters at Redshift $z \sim 0.2$

II: CFH12k Weak Lensing Analysis and Global Correlations ^{*}

S. Bardeau^{1,2}, G. Soucail¹, J.-P. Kneib^{3,4}, O. Czoske^{5,6}, H. Ebeling⁷, P. Hudelot^{1,5}, I. Smail⁸, and G. P. Smith^{4,9}

¹ Laboratoire d'Astrophysique de Toulouse-Tarbes, CNRS-UMR 5572 and Université Paul Sabatier Toulouse III, 14 Avenue Belin, 31400 Toulouse, France

² Laboratoire d'Astrodynamique, d'Astrophysique et d'Aéronomie de Bordeaux, CNRS-UMR 5804 and Université de Bordeaux I, 2 rue de l'Observatoire, BP 89, 33270 Floirac, France

³ Laboratoire d'Astrophysique de Marseille, OAMP, CNRS-UMR 6110, Traverse du Siphon, BP 8, 13376 Marseille Cedex 12, France

⁴ Department of Astronomy, California Institute of Technology, Mail Code 105-24, Pasadena, CA 91125, USA

⁵ Argelander-Institut für Astronomie, Universität Bonn, Auf dem Hügel 71, 53121 Bonn, Germany ^{**}

⁶ Kapteyn Astronomical Institute, P.O. Box 800, 9700 AV Groningen, The Netherlands

⁷ Institute for Astronomy, University of Hawaii, 2680 Woodlawn Dr, Honolulu, HI 96822, USA

⁸ Institute for Computational Cosmology, Department of Physics, Durham University, South Road, Durham DH1 3LE, UK

⁹ School of Physics and Astronomy, University of Birmingham, Edgbaston, Birmingham, B15 2TT, UK.

Received 09/03/07; accepted 09/05/07

ABSTRACT

Aims. We present a wide-field multi-color survey of a homogeneous sample of eleven clusters of galaxies for which we measure total masses and mass distributions from weak lensing.

Methods. The eleven clusters in our sample are all X-ray luminous and span a narrow redshift range at $z = 0.21 \pm 0.04$. The weak lensing analysis of the sample is based on ground-based wide-field imaging obtained with the CFH12k camera on CFHT. We use the methodology developed and applied previously on the massive cluster Abell 1689. A Bayesian method, implemented in the `Im2SHAPE` software, is used to fit the shape parameters of the faint background galaxies and to correct for PSF smearing. A multi-color selection of the background galaxies is applied to retrieve the weak lensing signal, resulting in a background density of sources of ~ 10 galaxies per square arc minute. With the present data, shear profiles are measured in all clusters out to at least 2 Mpc (more than 15' from the center) with high confidence. The radial shear profiles are fitted with different parametric mass profiles and the virial mass M_{200} is estimated for each cluster and then compared to other physical properties.

Results. Scaling relations between mass and optical luminosity indicate an increase of the M/L ratio with luminosity ($M/L \propto L^{0.8}$) and a $L_X - M_{200}$ relation scaling as $L_X \propto M_{200}^{0.83 \pm 0.11}$ while the normalization of the $M_{200} \propto T_X^{3/2}$ relation is close to the one expected from hydrodynamical simulations of cluster formation as well as previous X-ray analyses. We suggest that the dispersion in the $M_{200} - T_X$ and $M_{200} - L_X$ relations reflects the different merging and dynamical histories for clusters of similar X-ray luminosities and intrinsic variations in their measured masses. Improved statistics of clusters over a wider mass range are required for a better control of the intrinsic scatter in scaling relations.

Key words. Gravitational lensing – Dark matter – Galaxies: clusters: general – Galaxies: clusters: individual (A68, A209, A267, A383, A963, A1689, A1763, A1835, A2218, A2219, A2390)

Send offprint requests to: G. Soucail, soucail@ast.obs-mip.fr

^{*} Based on observations obtained at the Canada-France-Hawaii Telescope (CFHT) which is operated by the National Research Council of Canada, the Institut National des Sciences de l'Univers of the Centre National de la Recherche Scientifique of France, and the University of Hawaii.

^{**} Founded by merging of the Sternwarte, Radioastronomisches Institut and Institut für Astrophysik und Extraterrestrische Forschung

1. Introduction

Clusters of galaxies are potentially powerful probes for cosmology. They form the high-mass end of the mass function of collapsed halos, whose development as a function of redshift is a basic test of the hierarchical structure formation scenario and depends sensitively on a number of cosmological parameters (Eke et al. 1996; Voit 2005). The distribution of mass within

clusters forms another test of the non-linear development of structures (Navarro et al. 1997). The main difficulty in the application of these tests is to accurately measure total masses and the distribution of mass in clusters from observational proxies which are only more or less indirectly related to mass or the gravitational potential.

Several observational techniques are available to probe the mass distribution in clusters, each of them based on different physical assumptions and having its own strengths and weaknesses. Observation of the internal dynamics of clusters, based on the virial theorem and using the cluster galaxies as test particles of the cluster potential, is the “historical” approach, which provided early evidence for the existence of “missing” (now “dark”) matter (Zwicky 1937). However, clusters of galaxies are far from being simple relaxed systems and their structural complexity makes analysis of the velocity field difficult, as soon as the system shows substructure (Czoske et al. 2002).

Due to its dependence on the square of the electron density, X-ray emission from the hot intra-cluster gas (IGM) traces the deeper parts of the cluster potential and can be used to infer the total cluster mass under the assumption of hydrostatic equilibrium. It is known, however, that hydrostatic equilibrium alone provides an incomplete description of the physics of the IGM. X-ray observations with *XMM-Newton* and *Chandra* have revealed a wealth of complexity in the cluster X-ray emission (Markevitch & Vikhlinin 2007) which sign-post deviations from hydrodynamic equilibrium on various levels ranging from “sloshing” in apparently relaxed clusters to gross deviations in, e.g., cluster mergers (Finoguenov et al. 2005; Clowe et al. 2006). Nagai et al. (2007) show from simulations that mass estimates of relaxed clusters are biased low by 5 to 10% under the assumption that the gas is supported only by hydrostatic pressure; for unrelaxed clusters the situation is much worse. Hence, the usual X-ray observables like L_X or T_X do not provide the simple and expected robust mass estimators, although the newly introduced Y_X parameter (i.e. the product of T_X and $M_{g,500}$, Kravtsov et al. (2006)) shows some promise, with a low scatter when scaled with the mass.

The measurement of the Sunyaev-Zeldovich (SZ) effect is sensitive to the integrated pressure of the intra-cluster gas and is potentially a robust mass estimator (Grego et al. 2001; Bonamente et al. 2006). The new SZ interferometers like AMI (Barker et al. 2006, AMI collaboration) and millimeter bolometer arrays (e.g. LABOCA on APEX) are promising facilities for measuring the SZ effect in clusters, although their limited spatial resolution will limit the quality of cluster mass distribution.

Finally, weak gravitational lensing is most directly related to the gravitational potential and hence the total mass distribution; in particular, lensing does not rely on any assumptions concerning the physical state of the system. The main systematic effect afflicting lens mass measurements is that lensing measures projected masses, hence the interpretation of lensing measurements in terms of physical three-dimensional masses relies on certain assumptions concerning the spatial distribution of the matter. Projection effects can range from slight biases arising from triaxiality of the clusters or projection of the general large-scale structure (Metzler et al. 2001; King & Corless

2007; Corless & King 2007) to large errors in the mass estimates in cases where there are unrecognized line-of-sight mergers of clusters of comparable size (Czoske et al. 2002). Furthermore, there are calibration issues in the mass measurements coming from 1) the removal of instrumental effects acting on the galaxy shapes, 2) the calibration of the weak lensing signal, 3) the dilution of the signal by contamination with faint cluster or foreground galaxies, and 4) the uncertainties in the source redshift distribution. The first two issues have largely been addressed with simulated data in the STEP collaboration (Shear TEsting Program, Heymans et al. 2006) aimed at comparing many different weak lensing methodologies and identifying systematic effects in the respective methods. The last two issues can be addressed if additional information is available such as multi-color photometry and photometric redshifts or spectroscopic data.

From the above discussion it is clear that joint analyses of several types of observations are necessary if one wants to fully understand the structure of clusters of galaxies and the relation between different observables and mass estimates (Dahle et al. 2002; Cypriano et al. 2004). In practice, such an in-depth analysis can only be conducted for comparatively small samples of clusters, from which the relations and the scatter around the relations have to be empirically calibrated.

The aim of our program is to study a homogeneous sample of galaxy clusters using a variety of techniques to constrain their mass distribution. Smith et al. (2005) presented the results from strong lensing mass modeling of HST/WFPC2 observations of the central parts of the clusters and a comparison to X-ray temperatures measured by *Chandra*. Analyses of *XMM-Newton* observations of mostly the same clusters are presented by Zhang et al. (2007). In this paper, we present the weak lensing analysis of the cluster sample, using imaging data obtained with the CFH12k wide-field camera (Cuillandre et al. 2000) mounted at the Canada-France-Hawaii Telescope (CFHT); eleven clusters were observed in the *B*, *R* and *I* bands. The weak lensing analysis of the full sample of clusters follows the methodology presented previously by Bardeau et al. (2005, hereafter Paper I) who also applied it to the cluster A 1689.

This paper is organized as follows: Sect. 2 presents the cluster sample and gives a summary of the data reduction and the construction of catalogs that are used in the weak lensing and optical analyses of the clusters. In Sect. 3, we convert the galaxy shape measurements into two-dimensional mass maps which allow a qualitative assessment of the morphology of the dark matter distribution and comparison to the galaxy distribution in the clusters. In Sect. 4, we provide quantitative measurements of the cluster masses using one-dimensional radial fits to the weak shear signal. Sect. 5 discusses the light distribution of the clusters compared to the weak lensing mass in order to measure the mass-to-light ratio. We also compare the weak lensing masses to the X-ray properties of the clusters (luminosity and temperature) and normalize the $M-L_X$ and $M-T_X$ relations. We summarize our conclusions in Sect. 6 and discuss prospects for future weak lensing cluster surveys. Finally we give some details on the individual properties of the clusters in the appendix.

Throughout the paper we use $H_0 = 70 \text{ km s}^{-1} \text{ Mpc}^{-1}$, $\Omega_M = 0.3$, $\Omega_\Lambda = 0.7$. At a redshift of $z = 0.2$, $1''$ corresponds to 3.3 kpc and $1'$ to 200 kpc. Magnitudes are given in the Vega system.

2. Observations and data reduction

2.1. Description of the cluster sample

The clusters analyzed in this paper were selected from the XBACs catalog of Ebeling et al. (1996), a flux-limited compilation of Abell clusters detected in the ROSAT All-Sky Survey data. While the sample is thus based on the optically selected Abell catalog (Abell et al. 1989), which is known to be incomplete at high redshift and low mass, comparison with the X-ray selected BCS (Ebeling et al. 1998, 2000) shows that more than 74% of all BCS clusters are indeed Abell clusters. Since, for the very X-ray luminous systems considered here, this fraction rises to almost 90%, the optical preselection should not bias our sample. We select systems within the relatively narrow redshift range of $0.17 < z < 0.26$ in order to obtain an approximately luminosity-limited sample and to ensure that all clusters lie at about the same distance from the background population. Since X-ray luminosity is broadly correlated with cluster mass (Reiprich & Böhringer 2002), our sample is approximately mass limited, too. The redshift range quoted above was chosen to maximize the lensing efficiency for a background galaxy population at $\langle z \rangle \sim 1.0$ (Natarajan & Kneib 1997), thus defining the requirements in terms of limiting magnitudes. We applied further limits in declination ($-20^\circ < \delta < 60^\circ$ for accessibility with CFHT from Mauna Kea), Galactic latitude ($|b| > 20^\circ$ to minimize contamination by stars) and hydrogen column density ($N_H < 10 \times 10^{20} \text{ cm}^{-2}$) and from the remaining clusters randomly selected a sample of twelve clusters within a redshift dispersion $\sigma_z/z = 12\%$. Of these, eleven clusters were observed with the CFH12k wide-field camera (A773 could not be observed within the allocated nights). The same cluster sample was also imaged with the Hubble Space Telescope (HST) in order to measure the mass distribution in the cluster cores using strong-lensing techniques. Eight systems were observed by us with the WFPC2 camera (Program ID: 8249, PI Kneib), and data from observations of another two were retrieved from the HST archive (see Smith et al. 2005). Note that sample completeness is not of critical importance for this project which rather aims at compiling a homogeneous data set for a representative comparison among mass measurement techniques. Fig. 1 shows how our sample covers the high-luminosity region in the XBACs catalog.

Table 1 provides a summary of the cluster properties including global X-ray characteristics that will be used in our analysis.

2.2. Observations

Imaging data were obtained at the Canada-France-Hawaii Telescope during three observing runs in February 1999, November 1999 and May/June 2000 using the CFH12k camera, a mosaic of twelve $2k \times 4k$ CCDs (Cuillandre et al. 2000).

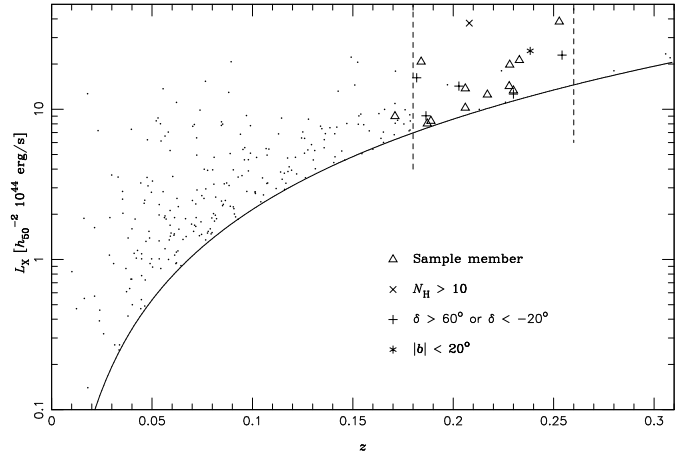


Fig. 1. L_X - z diagram for clusters from the XBACs catalog (dots). Triangles mark the 12 members of our sample, although one cluster (A 773) could not be observed and is not studied in this paper. The other symbols mark clusters which failed some of our secondary selection criteria. The solid line corresponds to an X-ray flux of $5 \times 10^{-12} \text{ erg s}^{-1} \text{ cm}^{-2}$, the flux limit of XBACs. The point outside the redshift limits (dashed lines) corresponds to the cluster A2218. Luminosities given here are the original XBACs luminosities from ROSAT All-Sky Survey data computed for $H_0 = 50 \text{ km s}^{-1} \text{ Mpc}^{-1}$, $\Omega_M = 1$, $\Omega_\Lambda = 0$.

With a pixel scale of $0''.206$ this camera covers a field of view of $42 \times 28 \text{ arcmin}^2$, i.e. about 1/3 of a square degree. Observations were conducted in three filters, B , R and I . A1835 was observed in V instead of B in February 1999 because the latter filter was not yet available at the time. Further observational details are given in Table 2.

We determine the limiting magnitude of each final image by computing the magnitude of a point source detected at 5σ in an aperture with diameter 1.45 times the full width at half maximum (FWHM) of the seeing disk. As shown by the CFH12k exposure time calculator (DIET¹) this is the optimal aperture within which 96% of the flux is integrated while the noise level remains sufficiently low. A point-like object detected at this significance level will have a magnitude error of about 20%. The resulting limiting magnitudes are included in Table 2. The *measured* magnitude limits corresponding to 50% completeness are found to be about 1.8 magnitudes brighter, partly due to the small apertures used in DIET.

During all three runs, the observing conditions were very good in terms of seeing (a prime requirement for weak-lensing studies) with the FWHM of stars consistently below $1''$ in the R band. The first and second observing runs were photometric; the third run was affected by cirrus (see Sect. 2.3).

2.3. Data reduction

Full details of the data reduction are presented in Czoske (2002). In Paper I we give a summary of the reduction process with special emphasis on the astrometric alignment of the exposures, which is of particular importance for the weak-lensing

¹ <http://www.cfht.hawaii.edu/Instruments/Imaging/CFH12K/DIET/CFH>

Table 1. Physical properties of the eleven clusters of the sample studied in this paper. The coordinates are those of the central galaxy as measured on the CFH12k images. The X-ray luminosities are taken from XMM-Newton measurements in Zhang et al. (2007) and are X-ray bolometric luminosities excluding the $< 0.1r_{500}$ region. The X-ray temperatures listed in column 6 were measured from Chandra data by Smith et al. (2005), excluding the very central regions where cool cores might be present in some of the clusters, except for A1689* (Andersson & Madejski 2004, XMM data) and A2390** (Allen et al. 2001). Column 7 lists the X-ray temperature measured with XMM-Newton from Zhang et al. (2007), except for A 2219*** for which we list the temperature obtained with ASCA (Ota & Mitsuda 2004) as no XMM data are available.

Cluster	RA (J2000)	Dec (J2000)	z	L_X (XMM) $10^{44} h_{70}^{-2} \text{ erg s}^{-1}$	T_X (Chandra) keV	T_X (XMM) keV
A 68	00 ^h 37 ^m 06 ^s .9	+09°09′24″	0.255	10.1 ± 0.9	9.5 ^{+1.5} _{-1.0}	7.7 ± 0.3
A 209	01 ^h 31 ^m 52 ^s .6	−13°36′40″	0.206	13.2 ± 1.1	8.7 ^{+0.6} _{-0.5}	7.1 ± 0.3
A 267	01 ^h 52 ^m 42 ^s .0	+01°00′26″	0.230	6.6 ± 0.7	6.0 ^{+0.7} _{-0.5}	6.5 ± 0.4
A 383	02 ^h 48 ^m 03 ^s .4	−03°31′45″	0.187	4.6 ± 0.5	5.2 ^{+0.2} _{-0.2}	5.3 ± 0.2
A 963	10 ^h 17 ^m 03 ^s .6	+39°02′50″	0.206	10.2 ± 0.9	7.2 ^{+0.3} _{-0.3}	6.3 ± 0.2
A 1689	13 ^h 11 ^m 30 ^s .1	−01°20′28″	0.184	21.4 ± 1.0	9.0 ^{+0.13} _{-0.12} *	8.4 ± 0.2
A 1763	13 ^h 35 ^m 20 ^s .1	+41°00′04″	0.228	15.9 ± 1.4	7.7 ^{+0.4} _{-0.4}	6.3 ± 0.3
A 1835	14 ^h 01 ^m 02 ^s .1	+02°52′42″	0.253	30.0 ± 1.4	9.3 ^{+0.6} _{-0.4}	8.0 ± 0.3
A 2218	16 ^h 35 ^m 51 ^s .5	+66°12′15″	0.171	12.2 ± 0.9	6.8 ^{+0.5} _{-0.5}	7.4 ± 0.3
A 2219	16 ^h 40 ^m 19 ^s .9	+46°42′41″	0.228	—	13.8 ^{+0.8} _{-0.7}	9.2 ± 0.4 ***
A 2390	21 ^h 53 ^m 36 ^s .9	+17°41′43″	0.233	28.9 ± 2.2	11.5 ^{+1.6} _{-1.3} **	10.6 ± 0.6

Table 2. Summary of the CFHT observations of our cluster sample. Exposure times are given in seconds. The seeing is measured as the FWHM of stars in the final stacked image for each cluster. The limiting magnitudes were computed following the DIET recipes (see text for details) for a point source detected at 5σ in an area of diameter 1.45 times the FWHM of the image. At this limit magnitudes are measured with an intrinsic error $\Delta m \sim 0.2$. They do not include the correction for galactic absorption which is given for each cluster in the 3 filters.

Cluster	B				R				I			
	Integr. time	Seeing	Limiting mag.	A_B	Integr. time	Seeing	Limiting mag.	A_R	Integr. time	Seeing	Limiting mag.	A_I
A 68	8100	1′1	26.4	0.40	7200	0′7	26.3	0.25	3600	0′6	25.3	0.18
A 209	7200	1′0	26.8	0.08	6600	0′7	26.3	0.05	3600	0′7	25.1	0.04
A 267	3000	1′0	26.0	0.11	4800	0′7	25.9	0.07	900	0′7	24.5	0.05
A 383	7200	0′9	27.0	0.14	6000	0′9	26.1	0.09	3600	0′7	25.1	0.06
A 963	7200	0′9	27.0	0.06	4800	0′8	26.1	0.04	10500	1′1	24.6	0.03
A 1689	3600	0′9	26.7	0.12	3000	0′8	26.1	0.07	3000	0′9	24.8	0.05
A 1763	3600	1′0	26.7	0.04	6000	0′9	26.2	0.02	3000	0′8	25.0	0.02
A 1835	3750 *	0′8	26.4*	0.10*	5400	0′7	26.5	0.08	3750	0′8	25.5	0.06
A 2218	3378	1′1	26.3	0.11	6900	1′0	26.2	0.07	3000	0′8	24.7	0.05
A 2219	5400	1′0	26.8	0.11	6300	0′8	26.4	0.07	3000	0′8	25.1	0.05
A 2390	2700	1′1	26.2	0.48	5700	0′7	26.3	0.30	3600	0′9	25.1	0.22

* V-band data for A 1835.

analysis of the images. We here provide additional information on the absolute photometric calibration of the images which will be relevant for the comparison of the total galaxy cluster luminosity to the total mass distribution presented in Sect. 5.

Before combining the exposures taken through the same filter for a given cluster we apply empirically determined photometric scaling factors to the exposures, which take into account differences in air mass and atmospheric transparency. The factors are determined by comparing the instrumental fluxes of several thousand stars in each image to the corresponding fluxes in a reference exposure (usually the exposure taken at the

lowest air mass). The median of the distribution of flux ratios is selected and used as the global scale factor which brings the exposure to the same level as the reference exposure. Remaining variations in the photometric zero point between chips (which have not been completely corrected by the twilight flat fields) are determined in a simpler manner using the sky levels in adjacent parts of neighboring chips. The intrinsic accuracy of the photometric calibration within the images is estimated to be on the order of 0.01 mag.

Plotting the relative scaling factors for the individual exposures against air mass allows the determination of the atmo-

spheric extinction if the series of exposures has been taken over a sufficient range in air mass; this is the case for several of our fields. We confirm that for the first and second of our observing runs the conditions were photometric throughout; the extinction coefficients determined in this way are in good agreement with the values listed on the CFH12k web site². The photometric zero points are determined from observations of photometric standard fields taken throughout the nights. We use the catalogs by Landolt (1992) supplemented more recently by Stetson (2000). Finally, the Galactic extinction is computed for each cluster from the maps of Schlegel et al. (1998), accessed through the NASA/IPAC Extragalactic Database (NED)³. Extinction corrections in R are typically on the order of 0.05 mag with the exception of Abell 68 and Abell 2390 for which we find values of up to 0.30 mag.

The third observing run was affected by intermittent thin cirrus and the conditions were not photometric. Calibrating the images taken during this run with standard observations is therefore likely to result in systematic errors in the photometric zero points. For the purposes of the present paper we adjust the zero points *a posteriori* by selecting stars from our fields and comparing their color distribution to external multi-color photometric sequences (Saha et al. 2005). In the $R - I$ vs. $B - R$ color plot the stellar sequence displays a characteristic knee from which photometric color corrections in $B - R$ and $R - I$ can be determined. A correction of 0.1 to 0.4 magnitudes is required for the clusters A1689, A1763, A2218, A2219 and A2390 to obtain a correct value for the $R - I$ color of elliptical galaxies. The correction terms are arbitrarily applied relative to the R -band which is taken as reference. Note that except for the color selection of cluster ellipticals or of “red” galaxies (see below for their definition), only the R -band luminosities, which are only mildly affected by the non-photometric conditions, are used in the rest of this paper. Only the clusters A 1763 and A 2219 suffered from significant absorption during the R -band observations, with an unknown absorption factor not higher than 0.3 mag.

2.4. Catalogs

From the corrected images, photometric catalogs are created for each cluster using SExtractor (Bertin & Arnouts 1996). Different catalogs are produced for the various measurements needed for the analysis. The details of the general methodology are given in Paper I and are summarized below. Object colors are computed using aperture magnitudes in circles of 3'' diameter, and stellar objects are identified using the tight relation in the magnitude vs. peak surface-brightness diagram.

Color-magnitude diagrams are constructed from the photometric catalog (Fig. 2), and the cluster red sequence is manually identified and approximated by a line with negative slope; all galaxies in a certain range around the line ($\Delta m = \pm 0.08$ typically) are stored in a catalog which we will refer to as the “elliptical galaxy” catalog. Since, for simplicity’s sake, we do

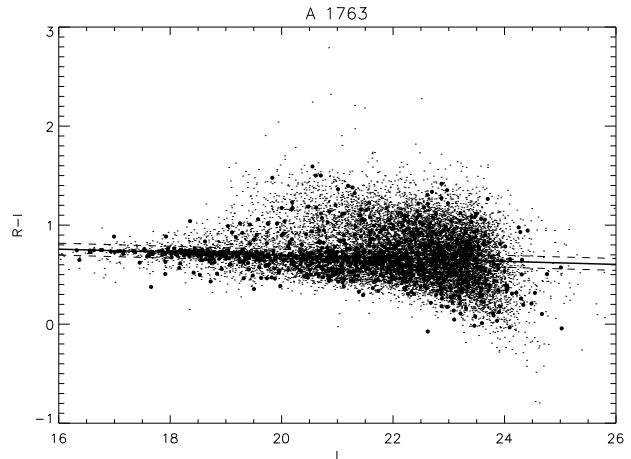


Fig. 2. Color-magnitude diagram for the cluster Abell 1763 showing the characteristic red sequence of elliptical cluster galaxies (width $\Delta m = \pm 0.06$). All galaxies redder than the sequence are included in the “red” galaxy catalog. The large dots correspond to galaxies within a radius of 250'' while the small dots come from the full catalog.

Table 3. Photometric properties of the sub-catalogs used in the weak-lensing analysis. Only R -band data are summarized. The magnitude range used for the faint galaxy selection is defined to be: $[m_R^* + 3.5 \text{ to } m_{\text{comp}} + 0.5]$, m_{comp} being the completeness magnitude of the catalog.

Cluster	m_R^*	Faint galaxies magnitude range	Mean number density (gal / arcmin ²)
A 68	19.04	[22.5–24.9]	22
A 209	18.41	[21.9–24.9]	24
A 267	18.71	[22.2–24.5]	17
A 383	18.12	[21.6–24.9]	22
A 963	18.41	[21.9–24.8]	23
A 1689	18.08	[21.6–24.8]	22
A 1763	18.67	[22.2–25.0]	24
A 1835	19.02	[22.5–25.4]	25
A 2218	17.91	[21.4–25.0]	21
A 2219	18.67	[22.2–25.3]	25
A 2390	18.75	[22.3–24.6]	18

not introduce any cut in magnitude, this catalog is affected by field contamination, especially at faint magnitudes.

For each cluster the photometric catalog is split into two sub-catalogs containing “bright” and “faint” galaxies, respectively. The magnitude cuts used to select these catalogs are scaled to the value of m^* , determined separately for each cluster and each filter (see Paper I for details and Table 3). The “faint galaxy” catalog is dominated by background sources and is used for the weak-lensing analysis. The galaxy density ranges from 22 galaxies/arcmin² in R to 14 galaxies/arcmin² in B and I . These numbers are averaged densities over the cluster sample and differ slightly from cluster to cluster due to cosmic variance. The “elliptical galaxy” catalog is defined in the photometric depth of the catalogs (Table 3).

² http://www.cfht.hawaii.edu/Instruments/Imaging/CFH12K/Summary/CFH12K_Differences.html

³ <http://nedwww.ipac.caltech.edu/>

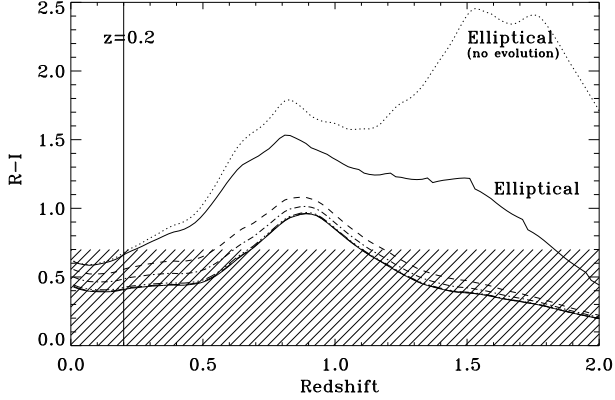


Fig. 3. Observed color index $R - I$ versus redshift for different spectral types, ranging from elliptical (with and without evolution, marked by full and dotted lines, respectively) to the bluest star-forming galaxies. We select “red galaxies” with $R - I > 0.7$ (outside the hatched region): The resulting catalog is next to free from foreground galaxies and cluster members, and is limited to $z \lesssim 1.8$. Synthetic spectral models are from Bruzual & Charlot (2003).

To further select faint background galaxies as well as to minimize cluster contamination, we add a simple color criterion to isolate galaxies above the cluster red sequence. As shown in Fig. 3, galaxies redder than $R - I \gtrsim 0.7$ should essentially be background galaxies ranging from the cluster redshift up to $z \approx 1.5 - 1.8$. This approach has already been successfully developed and used by several groups (Kneib et al. 2003; Broadhurst et al. 2005b) to eliminate or at least severely reduce the contamination of background galaxy samples by cluster galaxies. This extra criterion reduces the galaxy number densities to typically 8 – 10 galaxies/arcmin² (a reduction by a factor two compared to the “faint galaxy” catalogs, see Fig. 6). However, because the “red galaxy” catalog can be assumed to contain mostly background sources, we use this catalog for the remainder of our weak-lensing analysis, except in Sect. 3 where for practical reasons the “faint galaxy” catalogs are used as input.

2.5. Measurement of galaxy shape parameters

The shape parameters of faint galaxies are measured in all images, allowing a qualitative comparison between the different bands. However, in the end we only retain the measurements in the R band because the data quality in this band in terms of seeing and source density is superior to that of the other bands. In order to measure the galaxy shapes for the weak-lensing analysis, we correct them for PSF smearing using the IM2SHAPE software developed by Bridle et al. (2001). Details of the implementation are given by Heymans et al. (2006) as well as a comparison with more commonly used techniques such as the KSB scheme (Kaiser et al. 1995). Briefly, IM2SHAPE fits each object image with two concentric elliptical Gaussians convolved with a local estimate of the PSF, taking into account the background and noise levels. The local PSF is determined

as the average shape of the three stars closest to each object. Shape parameters and ellipticities with their error estimates are measured from the deconvolved object images using a Monte Carlo Markov Chain (MCMC) optimization technique.

2.6. Total optical luminosities of the clusters

There are several ways to estimate the total optical luminosities of the clusters from our wide-field images. In all cases, absolute luminosities include a k -correction obtained at the cluster redshift for an elliptical-type spectral energy distribution (Bruzual & Charlot 2003).

First, the total luminosity is integrated in circular annuli from the “bright galaxy” catalog and corrected for an average background luminosity computed in the external areas of the images. This is an easy way to compute luminosity and mass-to-light ratio profiles, as shown for A 1689 in Paper I. The main difficulty is the determination of the background contamination which is estimated from the average density far from the cluster. The measured values also strongly depend on the contamination from a few very bright foreground galaxies which appear in some cluster fields. To estimate the total luminosity of the cluster, it is necessary to correct for the magnitude cuts of the “bright galaxy” catalog. Assuming that the cluster galaxies follow a Schechter luminosity function, the correction factor, defined explicitly in Paper I, ranges from 10 to 30 percent, depending on the filter and depth of the individual images (for example in A 1689 the correction factor is 1.28 in B , 1.11 in R , 1.27 in I). The “total” luminosity of the clusters is then computed in a radius defined by the parameter r_{200} of the best fit model from McAdam (Sect. 4 and Table 5). We refer to this estimate of the total luminosity as L_R^{tot} in the rest of the paper.

We also use the “elliptical galaxy” catalogs, which we expect to be cleaner from non-cluster contamination, especially in the bright magnitude bins. Another advantage is that these catalogs are not limited at faint magnitudes and thus include most of the elliptical cluster members up to much fainter magnitudes than the “bright galaxy” catalogs. Therefore, no incompleteness factor is necessary in the integration. The correction for field contamination, again estimated from the average galaxy density outside the cluster and based on the same catalogs, is less dominated by bright galaxies than in the previous determination. Again, the total luminosity of the ellipticals is computed inside the virial radius r_{200} and is referred to as L_R^{ell} in the rest of the paper.

In practice, the field contamination from a few bright galaxies remains an issue for the total luminosity computed from the “bright” galaxies. We therefore use preferentially the luminosity of the elliptical galaxies of the clusters, which yields cleaner light-density maps with a more uniform background distribution. We check that the two luminosities do not differ strongly: the average ratio $L_R^{\text{tot}}/L_R^{\text{ell}}$ is 1.34, meaning that about 35% of the cluster luminosity are missed when only elliptical galaxies are considered. Of course, this ratio varies from cluster to cluster and is also sensitive to differences in the galaxy populations. Using L_R^{ell} only means that we assume that elliptical galaxies are best suited for tracing the galaxy content of the clusters and

its relation to the dark-matter distribution. Support for this assumption is provided by several studies showing a strong correlation between the light of early-type galaxies and the mass distribution derived from weak-lensing analyses (Smail et al. 1997; Clowe et al. 1998; Gray et al. 2002; Gavazzi et al. 2004).

3. Two-dimensional mass maps

We use an entropy-regularized maximum-likelihood technique, implemented in LENSENT2 (Marshall et al. 2002), to obtain mass reconstructions for each cluster based on the “faint galaxy” catalogs in the R band after PSF correction. Using the magnitude-selected “faint galaxy” catalog instead of the color-and-magnitude-selected “red galaxy” catalog does not change the global shape of the derived mass distribution. To avoid building under-dense regions with negative mass densities a mean background of $100M_{\odot}\text{pc}^{-2}$ is artificially added during the reconstruction. Since the mass distribution of clusters is extended, the individual values of the mass density as reconstructed with LENSENT2 are spatially correlated. The effective scale of this correlation is controlled by the *Intrinsic Correlation Function* (ICF) of the model which thus sets the resolution at which mass structures can be detected. We use an ICF of $180''$ ($\sim 600h_{70}^{-1}\text{kpc}$ at the cluster redshift) which represents a good compromise between detail and smoothness of the mass maps.

Figs. 4 and 5 show the results of the two-dimensional mass reconstructions around each cluster. In each plot the significance increases by 1σ between adjacent contours, with the lowest level representing a significance of 2σ above the mean background. For each cluster, σ is the average level of the noise peaks above the background, obtained from a randomization over the orientation of the “faint galaxy” catalogs used in the LENSENT2 mass reconstruction. 200 such random catalogs are produced for each cluster for the statistical analysis (see Paper I). The average value of σ for the entire sample is $\sigma_{\text{av}} \simeq 80M_{\odot}\text{pc}^{-2}$.

In all cases, the target cluster is detected at high significance. Table 4 gives the significance of the detection ν_{peak} in units of σ as defined above. Even for the least significant detection, A 267, the main peak is detected at about 3.6σ . A quantitative assessment of the reality of the mass clumps detected with LENSENT2 outside the main cluster component and at much lower nominal significance would require numerical simulations that are beyond the scope of this paper. We here use the mass maps solely to assess qualitatively the morphology of the cluster mass distributions (Table 4). We crudely classify the clusters as *circular* or *elongated* if the mass distribution within the $3\sigma_{\text{av}}$ contour has an ellipticity $(1 - b/a)$ smaller or larger than 0.2, respectively.

Also shown in Figs. 4 and 5 are contours of the light density of the “elliptical” galaxies as defined in Sect. 2.4. In Table 4 we indicate whether there is a good visual correlation between the mass and light distributions. Although these are rather qualitative criteria, most of the “elongated” clusters have both a mass and light distribution that is clearly not spherical.

Globally there is good agreement between the morphological information from our X-ray, strong- and weak-lensing anal-

yses, as well as the distribution of light in elliptical galaxies. We also find good agreement with the overall classification of Smith et al. (2005): the four clusters A 383, A 963, A 1689 and A 1835 correspond to the more relaxed and spherical clusters of the sample, while A 2219 and A 68 are also close to this category.

4. Weak-lensing masses

4.1. Selection of background galaxies

One of the main difficulties in obtaining reliable weak-lensing mass estimates is to ensure that only background galaxies are used in the analysis. The catalogs must be as free as possible from contamination from foreground or cluster galaxies to avoid attenuation of the weak-lensing signal, averaged in radial bins or locally, from galaxies with purely random orientations. The potential for such attenuation is largest near the cluster cores where the galaxy density is highest, causing the weak-lensing profiles to be flattened and the total masses to be underestimated. For a quantitative test of this effect, we create mock catalogs with the same density of sources as observed, distributed with random orientations and a Gaussian ellipticity distribution similar to the one observed after the PSF correction (Bardeau et al. 2005). These catalogs are then “lensed” by a cluster with an NFW mass profile, and average shear profiles are built in the same manner as for the observed catalogs (see below). The shear profiles are fitted by several mass profiles and the total cluster masses estimated in this way compared to the input cluster mass. To test the aforementioned attenuation effect contamination from cluster galaxies is added to the lensed catalogs, with a number density profile mimicking that of A 1689. The resulting mass profiles and total masses are again compared to the initial inputs. We find that even a 10% contamination by cluster members in the catalogs can cause the reconstructed total mass to be underestimated by up to 20 to 30%.

4.2. Fit of the shear profile

Two parametric mass profiles are used to fit the lensing data: a singular isothermal sphere (SIS) and an NFW profile (Navarro et al. 1997). The former is characterized by a single parameter, the Einstein radius θ_E or, equivalently, the velocity dispersion σ_v , while the latter is described by two independent parameters usually chosen as the scale radius r_s and the concentration parameter $c = r_{200}/r_s$. The virial mass M_{200} is computed as a function of the virial radius r_{200} and the critical density ρ_c of the Universe at the cluster redshift:

$$M_{200} = \frac{4}{3}\pi r_{200}^3 \times 200 \rho_c(z) \quad (1)$$

In order to determine the cluster mass distribution from the weak-lensing data we fit the shear pattern using McAdam, a Bayesian method developed by Marshall et al. (2002) and Marshall (2006). McAdam works directly on the PSF-corrected faint-galaxy catalogs without any radial binning of the data and is consequently more flexible than a fit of a few data points

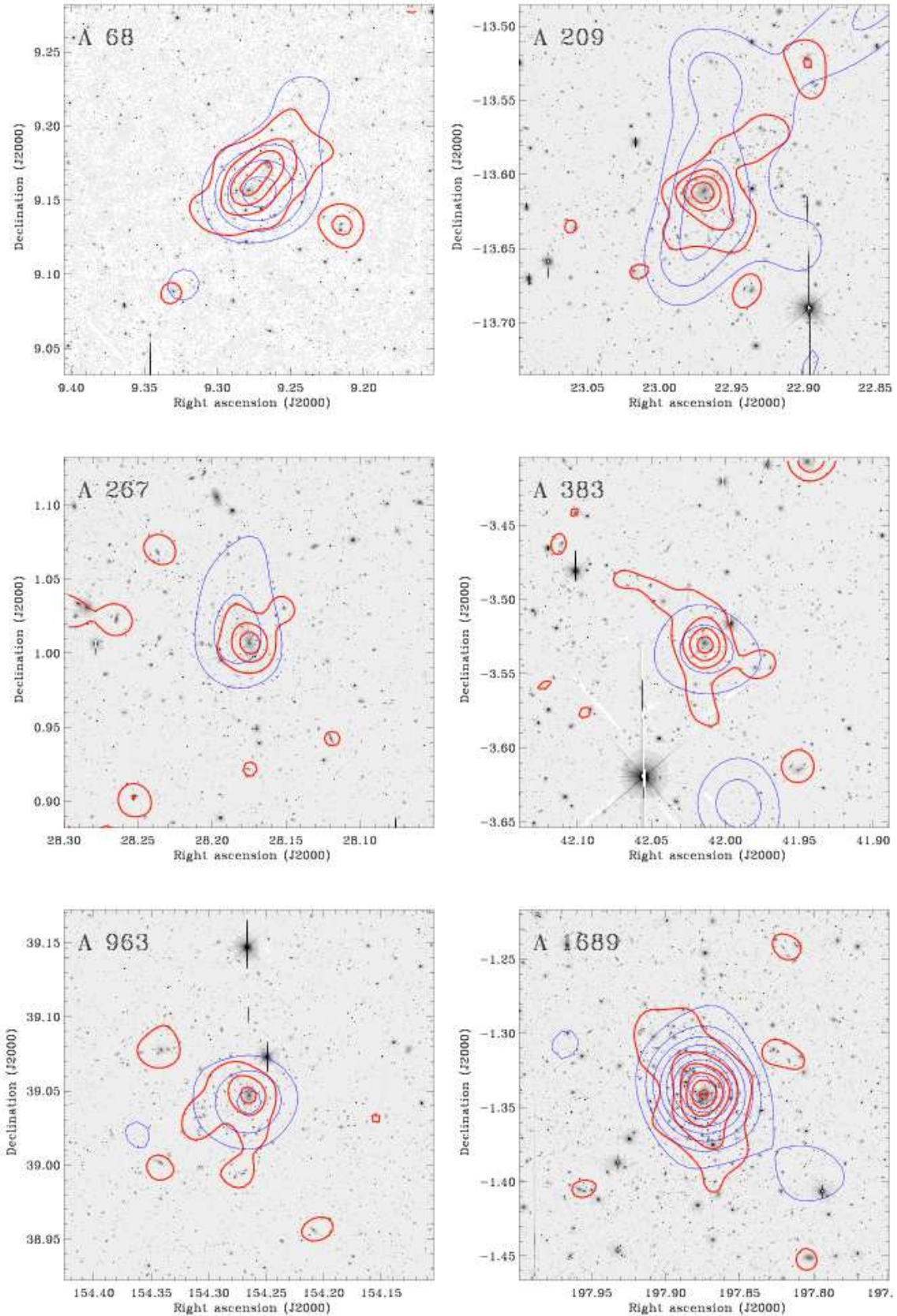


Fig. 4. $15' \times 15'$ CFH12k R -band images of the eleven clusters of the sample. Thick contours represent the light density of “elliptical” galaxies selected in the $R - I$ versus R color-magnitude diagram; thin contours represent the mass-density reconstruction from LENSENT2 (see text for details). The light contour levels are adjusted for each cluster according to its richness (or central density) and range from 2 to $3 \times 10^5 L_{\odot} \text{ arcmin}^{-2}$. Slight offsets between the positions of the mass peaks and the locations of the

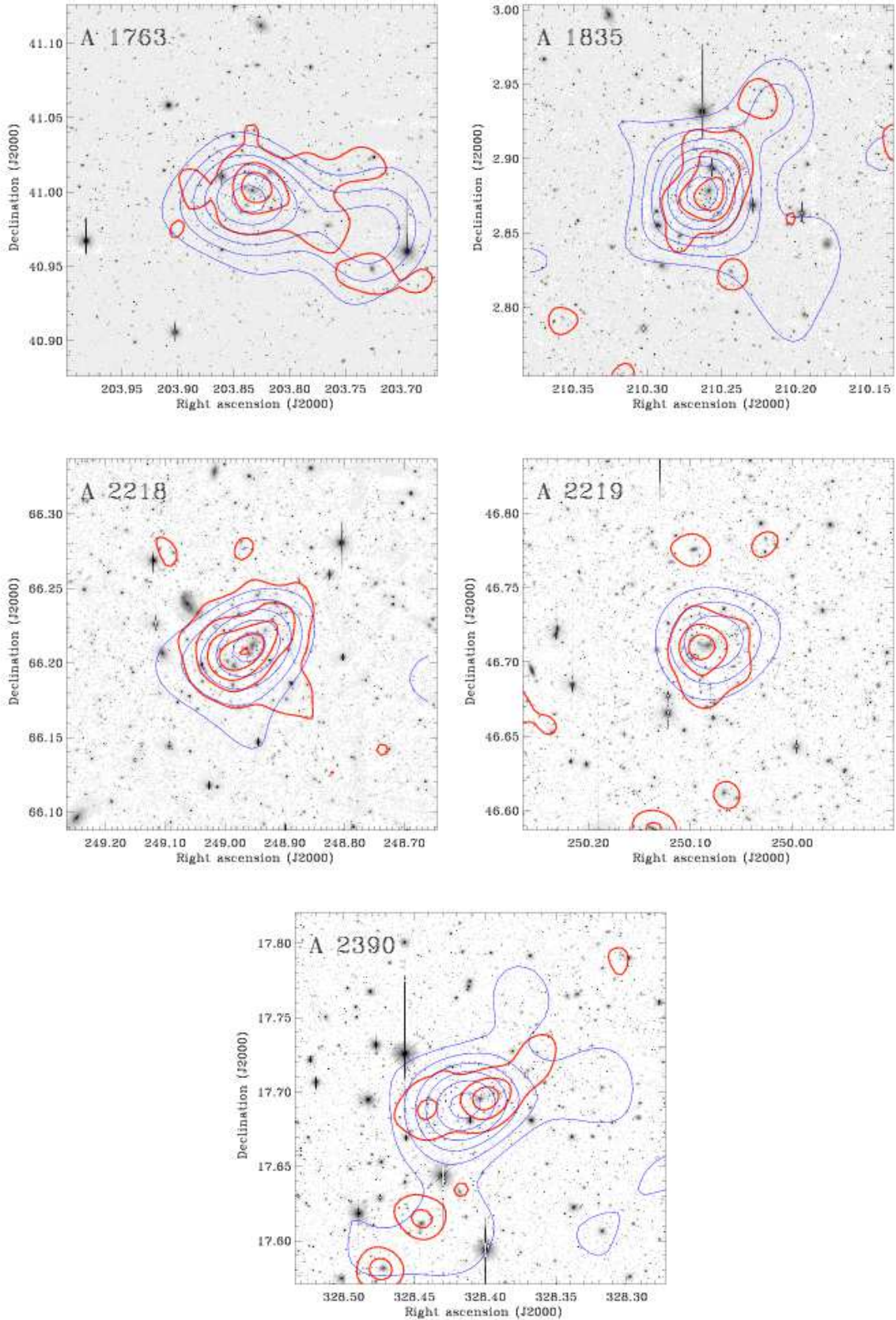


Fig. 5. Continued from Fig. 4.

Table 4. Global properties of the clusters in the sample: peak surface-mass density in terms of the standard deviation σ of the background fluctuations (col. 2); morphological characterization of the mass maps (col. 3); flag assessing the correlation between the mass maps and the light maps traced by the cluster ellipticals (col. 4); X-ray morphology as determined by Smith et al. (2005) (col. 5); “overall classification” assigned by Smith et al. (2005) based on HST lens modeling: for a cluster to be classified as “regular” it must contain a single mass component that is centered on the BCG, and the K -band luminosity of the BCG must contribute at least 50% of the cluster’s central K -band luminosity relative to the total cluster luminosity (col. 6).

Cluster	ν_{peak}	Mass morphology	M traces L ?	X-ray morphology	Overall classification
A 68	5.5	Circular	Y	Irregular	Unrelaxed
A 209	4.9	Elongated	N	Irregular	Unrelaxed
A 267	3.6	Elongated	N	Elliptical	Unrelaxed
A 383	3.6	Circular	Y	Circular	Relaxed
A 963	4.2	Circular	Y	Elliptical	Relaxed
A 1689	9.6	Circular	Y	—	—
A 1763	7.4	Elongated	Y	Irregular	Unrelaxed
A 1835	8.7	Circular	Y	Circular	Relaxed
A 2218	6.5	Elongated	Y	Irregular	Unrelaxed
A 2219	5.0	Circular	Y	Irregular	Unrelaxed
A 2390	7.4	Elongated	N	—	—

Table 5. Results of the mass-profile fits, obtained with McAdam and using the “red galaxy” catalogs only, for both the NFW and the SIS profiles. For all fits the cluster center is assumed to coincide with the location of the brightest cluster galaxy. The Einstein radius is computed at the average redshift of the background sources for each cluster (see text for details). M_{200} (also referred to as the virial mass) is the total mass included in a sphere of radius r_{200} . Also listed are the R -band luminosities of the clusters: L_R^{tot} is integrated within the “bright galaxy” catalog and corrected for incompleteness, while L_R^{ell} is the total luminosity of the “elliptical galaxies” selected within the color-magnitude sequence $R - I$ versus R . All luminosities are integrated within the virial radius r_{200} and error bars are based on the uncertainty of the r_{200} determination.

Cluster	c	r_{200} (h_{70}^{-1} Mpc)	M_{200} ($10^{12} h_{70}^{-1} M_{\odot}$)	σ_{shear} (km/s)	θ_E ($''$)	L_R^{tot} ($10^{12} h_{70}^{-2} L_{\odot}$)	L_R^{ell} ($10^{12} h_{70}^{-2} L_{\odot}$)
A 68	3.84 ± 1.13	1.49 ± 0.18	620 ± 197	880 ± 65	12.9 ± 1.9	6.6 ± 0.3	5.5 ± 0.3
A 209	3.00 ± 0.92	1.57 ± 0.17	719 ± 204	813 ± 70	12.4 ± 2.1	8.8 ± 0.7	7.6 ± 0.6
A 267	4.54 ± 2.01	1.15 ± 0.23	272 ± 146	634 ± 116	6.7 ± 2.4	5.3 ± 2.0	4.6 ± 1.7
A 383	2.62 ± 0.69	1.32 ± 0.17	419 ± 146	619 ± 72	7.4 ± 1.7	7.0 ± 2.5	4.9 ± 1.4
A 963	8.35 ± 1.25	1.33 ± 0.10	396 ± 90	812 ± 67	12.3 ± 2.0	5.9 ± 0.8	4.2 ± 0.5
A 1689	4.28 ± 0.82	2.25 ± 0.14	1971 ± 336	1277 ± 37	31.8 ± 1.8	12.8 ± 0.5	11.0 ± 0.4
A 1763	2.63 ± 0.63	1.93 ± 0.14	1386 ± 263	932 ± 60	15.0 ± 1.9	12.9 ± 0.8	10.0 ± 0.6
A 1835	2.58 ± 0.48	2.39 ± 0.14	2707 ± 414	1240 ± 47	26.6 ± 2.0	16.8 ± 0.8	12.1 ± 0.9
A 2218	6.86 ± 1.30	1.81 ± 0.14	971 ± 215	1040 ± 50	21.2 ± 2.0	12.8 ± 0.5	6.8 ± 0.3
A 2219	3.84 ± 0.99	2.25 ± 0.18	2094 ± 435	1175 ± 53	23.4 ± 2.1	14.6 ± 0.7	11.1 ± 0.8
A 2390	5.26 ± 1.43	1.74 ± 0.17	943 ± 246	1015 ± 54	18.1 ± 1.9	9.0 ± 1.1	6.6 ± 0.8

obtained by averaging within circular annuli. The output of McAdam is a probability distribution of the fitted parameters, which is obtained using a maximum-likelihood estimator and a MCMC iterative minimization. We use McAdam on the “red galaxy” catalogs and fit the mass distribution of each cluster with a single component, leaving the mass profile parameters (θ_E for SIS, c and M_{200} for NFW) as free parameters. A prior on the concentration parameter c is included with $2 < c < 10$, following the results of N-body simulations of cosmological structure formation at the galaxy cluster scale (Bullock et al. 2001; Hennawi et al. 2007). As discussed before, any residual contamination of the catalog by cluster galaxies, in particular in the central area, may reduce the central shear signal and thus

flatten the deduced mass profile. As no strong-lensing information is included, we add a prior on the lens center by assuming it to coincide with the position of the brightest cluster galaxy (BCG). This reduces the number of free parameters in the global fitting but is of little consequence for the final value of the total mass because the results of the fits are dominated by the shear signal at large distance from the cluster center. In addition to obtaining a global fit, we also compute for each cluster the radial shear profile which allows a straightforward assessment of the strength of the detected shear signal. The eleven shear profiles derived from the “red galaxy” catalogs are shown in Appendix A. A detailed cluster by cluster comparison with previous mass estimates from independent weak lensing stud-

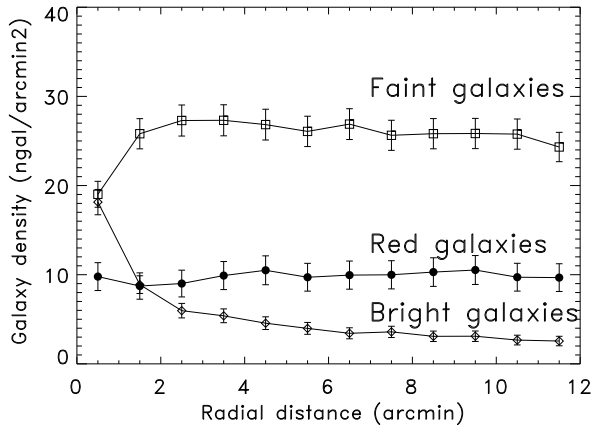


Fig. 6. Mean radial profile of the “red” galaxies, averaged over the four “relaxed” clusters (A 383, A 963, A 1689, and A 1835). Also plotted is the mean radial profile for the “bright” galaxies, representing the cluster members complementing the “faint” galaxy sample. As expected the “red” galaxy profile is flat and therefore mostly free from cluster contamination. The central dip in the faint galaxies profile may be partly due to the magnification bias acting on the background sources and also to obscuration effects caused by contaminating bright galaxies (not corrected).

ies is also included in this Appendix. In general, there is good agreement between our measurements and previous ones, except in a few cases like A 1689 where there is a wide range of measured weak lensing masses, using different methods. The most recent ones seem to converge to a value close to the one presented in this paper. Note also that seven out of our eleven clusters were imaged by Dahle et al. (2002) who fitted their radial shear profiles with SIS profiles. Most of the clusters have a best-fit value of the velocity dispersion σ_{sh} much higher than the present one, but their analysis was based on shallower data taken in a much smaller field of view and so has much larger systematic and random errors than our analysis.

The emphasis of the work presented here is on the total mass of the clusters. The resulting best fits as well as the internal errors are summarized in Table 5. Given the correlated nature of the parameters in our analysis and the weakness of some of the detections, we focus our discussion on our estimates of the virial radius r_{200} and the virial mass M_{200} which are robust results of the weak-lensing analysis. Combining strong- and weak-lensing effects increases the accuracy of the mass reconstruction close to the center and the fit of the concentration parameter c of the NFW profile (Broadhurst et al. 2005b) but requires modifications of the likelihood estimators used by McAdam in the central areas. Results from a high-resolution study based on this approach will be presented in a forthcoming paper (Hudelot et al., in preparation) and will also allow us to discuss the distribution of values measured for the concentration parameter c across the sample as well as its cosmological consequences.

Fitting the shear profile with the SIS mass profile yields a velocity dispersion σ_{shear} which can be converted into an

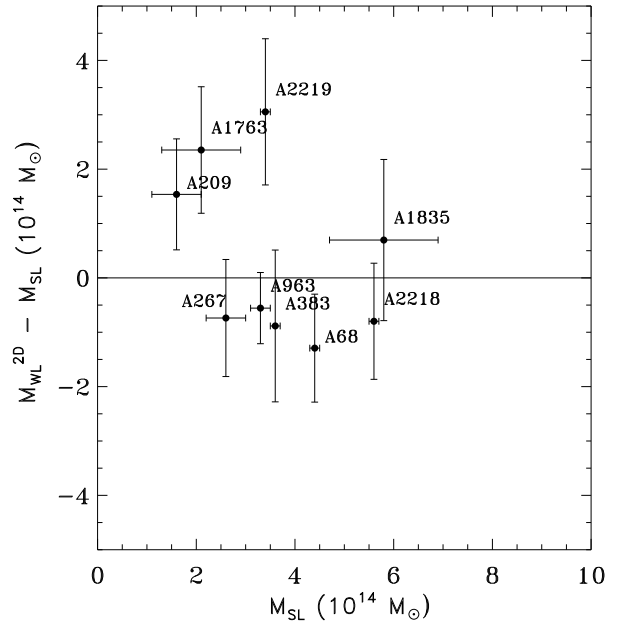


Fig. 7. Projected mass enclosed within a radius of $500 h_{50}^{-1}$ kpc derived from the strong-lensing analysis of Smith et al. (2005) versus the difference between the weak- and strong-lensing masses measured in the same aperture. The weak-lensing masses have been converted to an Einstein-de Sitter cosmology with $H_0 = 50 \text{ km s}^{-1} \text{ Mpc}^{-1}$ to allow a direct comparison with the strong-lensing masses.

Einstein radius θ_E using the value of the ratio $D_{\text{LS}}/D_{\text{OS}}$ averaged over all the sources with redshifts estimated from their photometric properties (Bardeau et al. 2005). θ_E does not depend strongly on the exact value of z_S which turns out to be $z_S \approx 1.1$ for all clusters. We stress that errors due to differences in the redshift of the background population from cluster to cluster are negligible as we selected the clusters to lie in a narrow redshift range so that the scaling factor $D_{\text{LS}}/D_{\text{OS}}$ varies by less than 5% from cluster to cluster. A global error on the mean redshift of the sources may introduce a systematic shift of the scaling factor and hence the total mass, but its variation with $\langle z_S \rangle$ is so small that this cannot account for more than a few percent, provided the sources are at redshift at least twice the lens redshift.

A direct comparison between the masses from our weak-lensing analysis and the masses measured by Smith et al. (2005) is presented in Fig. 7. The strong-lensing “total mass” is in fact the projected mass enclosed within a radius $R = 500 h_{50}^{-1}$ kpc, extrapolated from the strong-lensing modeling, whereas the virial mass M_{200} is measured in a sphere of radius r_{200} which varies from cluster to cluster. In order to account for these differences we compute the projected mass inside the projected radius $R = 500 h_{50}^{-1}$ kpc using the NFW parameters determined from the weak-lensing best fit, following the relation

$$M_{\text{WL}}^{2\text{D}}(< R) = 2\pi r_s^2 \Sigma_{\text{cr}} \int_0^{R/r_s} \kappa(y) y dy \quad (2)$$

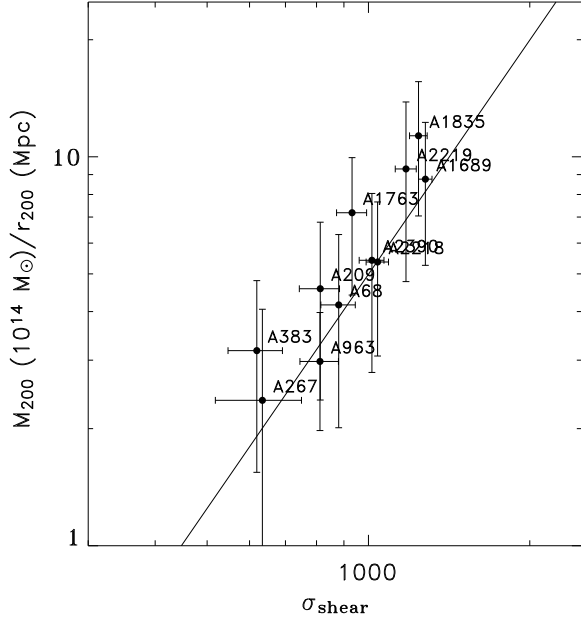


Fig. 8. Comparison between the total mass M_{200} divided by the virial radius r_{200} and the velocity dispersion of the fitted SIS model. The straight line corresponds to $M_{200}/r_{200} \propto \sigma_{sh}^2$ and confirms the correspondence between the two mass estimates (see text for details).

with $r_s = r_{200}/c$. The integral has been computed by Bartelmann (1996) and Wright & Brainerd (2000) and the projected mass can be rewritten in terms of the virial mass M_{200} and the concentration parameter c as

$$M_{WL}^{2D}(< R) = \frac{M_{200}}{\ln(1+c) - c/(1+c)} \mathcal{F}\left(\frac{R}{r_s}\right) \quad (3)$$

with $\mathcal{F}(x)$ defined as

$$\mathcal{F}(x) = \begin{cases} \frac{2}{\sqrt{1-x^2}} \operatorname{artanh} \sqrt{\frac{1-x}{1+x}} + \ln\left(\frac{x}{2}\right) & (x < 1) \\ 1 + \ln\left(\frac{1}{2}\right) & (x = 1) \\ \frac{2}{\sqrt{x^2-1}} \arctan \sqrt{\frac{x-1}{x+1}} + \ln\left(\frac{x}{2}\right) & (x > 1) \end{cases} \quad (4)$$

The comparison between the two masses is shown in Fig. 7 and shows good agreement. No obvious bias appears in the sample although there seems to be a dichotomy between two families of clusters. A 209, A 1763 and A 2219 have weak-lensing masses that appear to be overestimated in comparison with those of the other clusters. By contrast, the three clusters identified as “relaxed” clusters both in the weak- and in the strong-lensing analysis (A 383, A 963 and A 1835) show good agreement between the two mass measurements.

In order to check the validity of our mass estimates, we also compared masses deduced from the radial fits of the two different parametric models (NFW and SIS). The total mass

enclosed within the virial radius is M_{200} for the NFW profile and is proportional to $\sigma_{shear}^2 \times r_{200}$ for the SIS profile. Fig. 8 compares these two quantities which show on average the same behavior, so we are confident that using either the virial mass or the mass deduced from the isothermal profile does not change the validity of the scaling relations discussed below. Note that in both cases we use the 3D total mass enclosed within the virial radius r_{200} .

5. Global correlations

With all measurements in hand we now investigate the correlations between the lensing mass and immediate cluster observables like the optical luminosity or X-ray characteristics such as luminosity and temperature.

5.1. Correlations between mass and optical cluster properties

Mass and luminosity are strongly correlated quantities as can be seen in Fig. 9. The M/L ratio is usually representative of the dynamical state of a cluster and is a tracer of its star-formation history. One of the current issues of cluster research is whether the M/L ratio is a constant and universal value at least for rich clusters, or whether it increases with mass, as recently suggested by, e.g., Popesso et al. (2005).

We here compute the M/L ratio as the virial mass within the virial radius r_{200} (M_{200}) divided by the luminosity L_R^{ell} as defined above. We use the virial mass instead of the 2D projected mass M_{200}^{2D} because the latter depends on the concentration parameter c , which is poorly constrained in our study. We, however, convince ourselves that changing c from 2 to 10 decreases the deduced projected mass by only less than 20%. The optical cluster luminosities are carefully corrected for background contamination as well as Galactic extinction and are also k -corrected. We do not apply any correction for luminosity evolution which is likely to be small at the low redshift of our target clusters. To obtain a global M/L ratio for all clusters we apply the average correction factor to the total luminosity, 1.34. In practice, we find an average value for the whole cluster sample before correction for the total luminosity

$$\langle M/L_R^{ell} \rangle = (133 \pm 50) h_{70} (M/L)_\odot \quad (5)$$

or globally for all galaxies

$$\langle M/L_R^{tot} \rangle = (100 \pm 38) h_{70} (M/L)_\odot. \quad (6)$$

These values are close to the value of $M/L_V^{all} = 180_{-110}^{+210} h (M/L)_\odot$ obtained by Smail et al. (1997) in their early weak-lensing study of a sample of rich clusters. On the other hand, Carlberg et al. (1996, 1997) find an average value of $\langle M/L_r \rangle = (289 \pm 50) h_{100} (M/L)_{r_\odot}$ for the M/L ratio of rich clusters from the CNOC survey (a sample of 14 clusters spanning a redshift range [0.17–0.54]). Theirs are, however, global dynamical values which overestimate the M/L ratio measured at the virial radius r_{200} by approximately 20% (Carlberg et al. 1997). Although, all considered, their average M/L ratio is still higher than the one found in our analysis, the discrepancy is

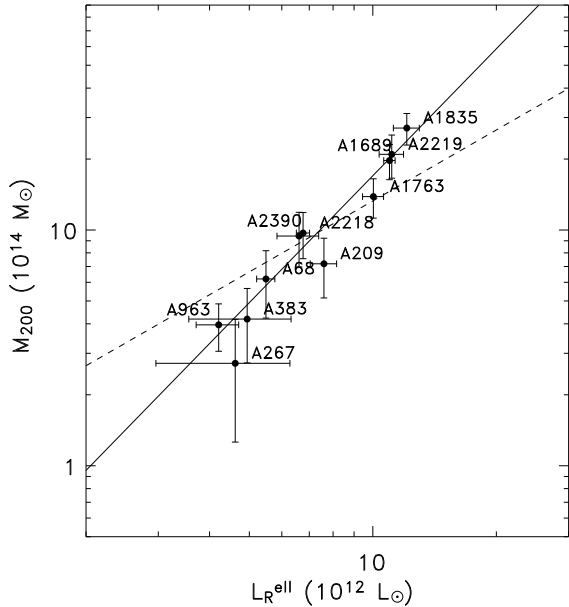


Fig. 9. Mass versus optical luminosity for the clusters in our sample. The mass is computed at the virial radius r_{200} derived from the best weak-lensing fits obtained with McAdam. The optical luminosity is computed in the R band for the “elliptical” galaxies only, selected from the color-magnitude relation, and has been corrected for background contamination. Both quantities are projected (i.e. integrated along the line of sight) and are therefore comparable. The dashed line represents a constant M/L ratio of 133 in solar units while the solid line represents the best-fit power law $M \propto L^{1.8}$.

barely significant when all sources of error are taken into account. For A 2390, the only galaxy cluster in common between the two samples, the velocity dispersion as well as the M/L point toward a higher mass than the weak lensing mass measured in this paper. However, their determination of the virial radius differs significantly from ours. As a consequence, the virial mass and the total luminosity are not measured in the same area and the comparison is not conclusive.

If we drop the assumption of a constant M/L ratio for clusters, Fig. 9 shows a strong correlation between mass and light, steeper than for a constant M/L , with massive clusters having higher M/L ratios. A log-log fit of the mass-luminosity relation, including errors on the mass measurements shows a power law dependence with an index $\alpha = 1.80 \pm 0.24$, or equivalently $M/L \propto L^{0.80 \pm 0.24}$.

The tendency of increasing M/L ratio with virial mass is significant, even though the mass range of the present sample is rather limited. Previous analyses have already shown similar trends, in particular in a detailed comparison between dynamical mass estimates from the SDSS and luminosities coming from either optical or X-ray measurements (Popesso et al. 2005). Their sample spans a wide mass range, from groups up to massive clusters, and although there is a large dispersion of their data points, the correlation between M/L and

mass is confirmed, but with a lower slope than in the present study. However, although the mass range of their sample is wider than ours their dynamical mass determination may not be as accurate as the weak lensing masses in the present analysis. Complementary lensing mass measurements for lower mass clusters have been obtained by Parker et al. (2005) using the CNOC galaxy groups. They show some evidence for an increase in the M/L ratio from poor to rich galaxy groups. This result is in agreement with theoretical predictions obtained by comparing the Press-Schechter mass function with the observed luminosity function (Marinoni & Hudson 2002). The M/L ratio in the high mass range, typical of rich clusters of galaxies, scales as $L^{0.5 \pm 0.26}$, in close agreement with our observations. However, Marinoni & Hudson (2002) assumed a rather high value of $\sigma_8 = 0.9$. Following the latest WMAP3 analysis, a lower $\sigma_8 = 0.75$ might change their $M-L_{\text{opt}}$ relation by lowering the normalization but not the power-law exponent (Reiprich 2006).

This scaling behavior is predicted in semi-analytical models of galaxy formation and has been interpreted as a decrease in galaxy formation efficiency in rich and dense environments due to the long cooling time of hot gas (Kauffmann et al. 1999). Indeed, recent X-ray observations have shown that in the centers of dense clusters the gas cools less efficiently than predicted by the standard cooling flow model (Peterson et al. 2001; Fabian et al. 2003). By injecting energy in the form of radio jets, AGN may be responsible for switching off cooling at the centers of massive haloes, thus preventing the formation of very bright structures (Bower et al. 2006). Also, star formation is quenched in newly infalling galaxies through a variety of physical processes, some of which, e.g. ram pressure stripping of gas, are the more efficient the denser the environment (e.g. Treu et al. 2003).

5.2. Correlation between optical and X-ray luminosities

There is some correlation between the clusters’ optical and X-ray luminosities, although the luminosity range is not very extended in our sample of bright X-ray clusters. Popesso et al. (2005) performed linear fits between these quantities using a large sample of low-redshift groups and clusters of galaxies from the RASS-SDSS Survey over more than two decades in luminosities. For the correlation between optical and X-ray luminosities, they find a best fit law:

$$\log(L_{\text{opt}}/10^{12}L_{\odot}) = 0.64 \log(L_X/10^{44} \text{ erg s}^{-1}) + 0.45 \pm 0.15.$$

Instead of doing similar fits with our sample, which may have little physical meaning, we simply compare the averaged optical luminosity ($L_R^{\text{tot}} = 10.2 \times 10^{12} L_{\odot}$) at the mean X-ray luminosity of the sample ($\langle L_X \rangle = 10.5 \times 10^{44} \text{ erg s}^{-1}$). This value corresponds closely to the value predicted by the relation of Popesso et al. (2005). We therefore confirm their normalization from an independent sample with great accuracy and demonstrate that this normalization does not change out to $z \sim 0.2$ at high L_X .

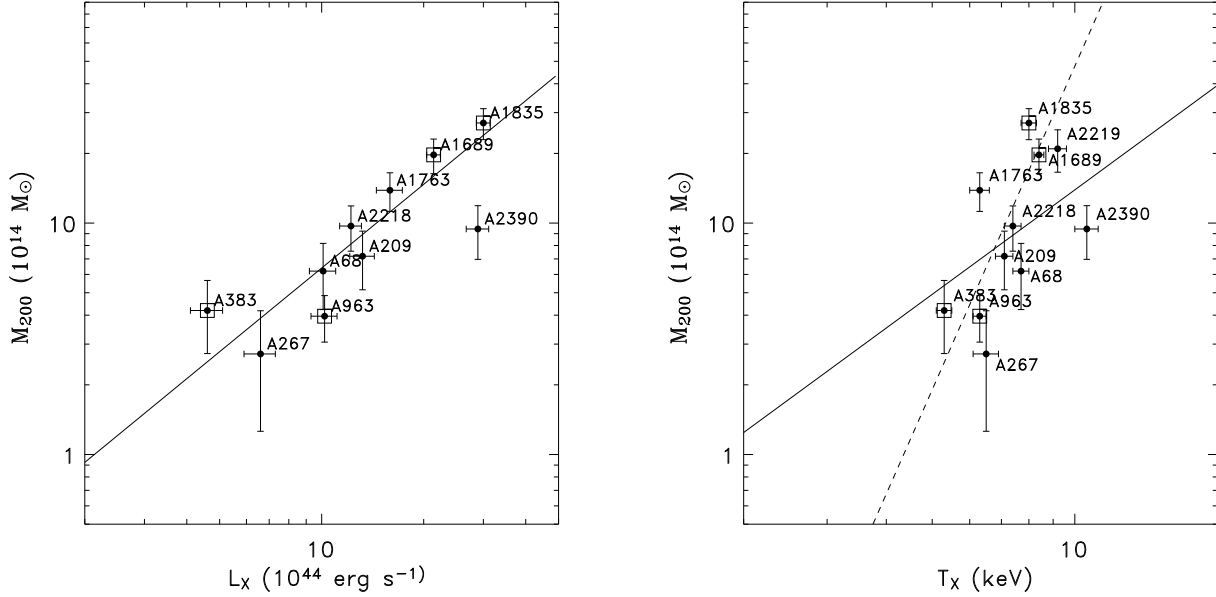


Fig. 10. *Left:* Weak lensing 3D virial mass M_{200} versus X-ray luminosity. The best fit line has a slope $\alpha = 1.20 \pm 0.16$ and is discussed in the text. *Right:* Weak lensing 3D virial mass M_{200} versus X-ray temperature. The straight line corresponds to a $M_{200} \propto T^{3/2}$ relation while the dashed line corresponds to the best fit power law relation $M \propto T^{4.6 \pm 0.7}$. The virial mass M_{200} is derived from the best weak lensing fits obtained with McAdam, temperatures are derived from XMM data (Zhang et al. 2007), completed by ASCA data from (Ota & Mitsuda 2004) for A 2219. In both plots, the 4 clusters with cooling core or relaxed properties are marked with empty boxes.

5.3. Correlation between cluster mass and X-ray luminosity

We now compare the deprojected mass derived from the weak lensing analysis with the cluster X-ray properties. We consider the virial mass M_{200} enclosed within r_{200} , the result of the weak lensing best fit performed with McAdam. Bolometric X-ray luminosities are measured from XMM-Newton data and integrated up to $2.5r_{500}$, a radius which is close to twice our virial radius r_{200} (Zhang et al. 2007). They are listed in Table 1. Fig. 10 shows the correlations between M_{200} and the cluster X-ray properties. A linear regression between mass and luminosity (including errors in both axes in log-log space) gives the scaling relation

$$M_{200}/10^{12} M_{\odot} = 40_{-15}^{+23} \left(L_{X,\text{bol}}/10^{44} \text{ erg s}^{-1} \right)^{1.20 \pm 0.16}. \quad (8)$$

As the slope is close to 1, one may also consider a constant mass to (X-ray) light ratio for which we obtain an average value of $M/L_X = 67 \pm 24$ in units of $(10^{12} M_{\odot}/10^{44} \text{ erg s}^{-1})$. Inverting the $L_X - M$ relation gives

$$L_{X,\text{bol}}/10^{44} \text{ erg s}^{-1} = 2.16_{-0.53}^{+0.71} \left(M_{200}/10^{14} M_{\odot} \right)^{0.83 \pm 0.11} \quad (9)$$

which seems in contradiction with some previous determinations of the correlation between mass and X-ray luminosity where the slope of the $L_X - M$ relation is on the order of 1.3 to 2.0 (Reiprich & Böhringer 2002; Popesso et al. 2005; Maughan 2007). From the theoretical point of view, a relation $L_{\text{bol}} \propto M^{4/3}$ is expected in a self-similar model for clusters, while including “pre-heating” in the physical processes

of cluster formation leads to a relation given by $L_{\text{bol}} \propto M^{11/6}$ (Evrard & Henry 1991). An accurate determination of the observed $L_X - M$ relation is quite difficult with our present mass estimates, also because the perturbation induced on the measurements by the central cooling core of some clusters modifies the sample properties. Note also that our present normalization of the $L - M$ relation is only 60% higher than the one determined by Maughan (2007), contrary to the normalization found by Popesso et al. (2005) which is lower than our value by a factor of 3 at $10^{15} M_{\odot}$ but their $L - M$ relation presents a very different slope, close to 2 when using bolometric X-ray luminosities. Going further in this analysis is presently difficult because of the limited size and the small mass range of our sample. In addition, our sample is X-ray flux-limited which may introduce some bias into the relations involving L_X , because for a given mass, only the high luminosity clusters are selected (Reiprich 2006).

5.4. The mass-temperature relation

The X-ray temperatures have been measured on detailed XMM observations (Zhang et al. 2007). The global values are the results of the volume averaged radial temperature profiles between $0.2 - 0.5r_{200}$. As shown in Fig. 10, we presently have too large uncertainties and dispersion in the measurements to correctly fit a power law for the $M - T$ relation. Instead, we

simply fix the slope to what is expected if clusters are in hydrostatic equilibrium, $M \propto T^{3/2}$. Then we find a normalization

$$M_{200}/10^{14}M_{\odot} = 0.44^{+0.39}_{-0.21} \left(\frac{T_X}{1 \text{ keV}} \right)^{3/2}. \quad (10)$$

This normalization deserves some comment because it is one of the few attempts at fixing it with weak lensing mass measurements. Pedersen & Dahle (2006) also provided a tentative determination of the $M - T$ relation with weak lensing masses. From their whole sample of rich clusters, spread over a large redshift range, they find

$$M_{8\text{keV}} = (0.78 \pm 0.14) \times 10^{15} h^{-1} M_{\odot}.$$

The normalization translates to a value of 0.49 ± 0.09 in our units (Eq. 10) and is in very good agreement with the present work. Our value is also quite close to a recent prediction obtained from a sample of simulated clusters realized with the most recent implementation of the Tree-SPH code GADGET2 (Springel 2005). For the most massive clusters, Ascasibar et al. (2006) find a $M - T$ relation of

$$M_{200}/10^{14}M_{\odot} = 0.473 h_{70}^{-1} \left(\frac{T_X}{1\text{keV}} \right)^{3/2}, \quad (11)$$

also in good agreement with our result, although their relation is established at $z = 0$. However, the authors claim that their normalization is lower than the values found in previous simulations and explain this partly by improvements of the treatment of entropy conservation.

5.5. Discussion

The scatter in the $M - T$ and $L - T$ relations should be representative of the diversity in the cluster histories but it is not easy to analyze because our sample is small. The individual mass measurements still have large uncertainties associated to the weak lensing method: masses are underestimated if the catalogs are not completely cleaned from foreground or cluster contamination and the low density of background sources used for the weak lensing reconstruction adds another source of noise which strongly limits the accuracy of the measurements. These systematic uncertainties, which are difficult to quantify without detailed simulations of mock catalogs, are presently not taken into account in this analysis. The remaining uncertainty on the concentration parameter adds at least another 20% uncertainty on the total mass, included in our present mass errors budget. All in all, weak lensing masses cannot presently be determined with accuracy better than 40 to 50%. However, the tight correlation between mass and optical luminosity suggests that some of these biases partly cancel when measuring the mass or the total luminosity; this is the case for all geometric departures from spherical symmetry (ellipticity of the light/mass distributions or projection effects). Systematic biases in the mass determinations should not change the slope of the scaling relations dramatically while some uncertainty in their normalization remains. But since the slopes of the $L_X - M$, $T_X - M$ and $L_{opt} - M$ relations are all shallower compared to previous results, we may also suspect some scale dependant biases, most

probably at the low mass end of our sample, where the weak lensing measures are the most difficult to characterize. Further improvements in the weak lensing methodology are in progress and may help clarifying this possible bias.

Moreover, although the sample was initially selected for its homogeneity, at least in X-ray properties ($L_X > 4 \times 10^{44} h_{70}^{-2} \text{ erg s}^{-1}$), at least three out of the eleven clusters (i.e. about 25% of the sample) present a strong central cooling core (namely A 383, A 963 and A 1835) which perturbs the total X-ray luminosity (clusters are overluminous) and the X-ray temperature (clusters are too cool) for a given mass. This effect is partly taken into account in the way Zhang et al. (2007) measured the X-ray temperatures, excluding the X-ray signal in the central core ($r < 0.2r_{500}$). Another five clusters show signs of non-sphericity in the mass distribution. Following Popesso et al. (2005) we suspect that most of the dispersion in the scaling relations is due to the intrinsic dispersion on the X-ray properties of these rich clusters although the present mass uncertainties add a significant fraction of the total scatter. For the optical luminosity of clusters the link with the total mass is tighter. This is an indication that early-type galaxies are good tracers of the mass in clusters and that the dispersion in M with T_X is real.

6. Conclusions

We have presented the first weak-lensing analysis of a homogeneously selected sample of eleven X-ray luminous clusters in a narrow redshift slice at $z \sim 0.2$. Using wide-field imaging in three bands (B , R and I) covering up to 5 Mpc in radius around the cluster targets we are able to disentangle between foreground, cluster and background galaxies. The weak lensing signal is always well detected up to 2 Mpc, but generally extends out to the edge of the field at lower signal-to-noise.

The weak lensing methodology used in the paper has already been tested and validated on the cluster A 1689 which yields the highest signal-to-noise detection in our sample (Bardeau et al. 2005). To measure galaxy shapes and correct them for PSF anisotropy and circularization, we used the IM2SHAPE tool. Our reliance on IM2SHAPE is justified by the results of the Shear Testing Program (STEP, Heymans et al. 2006) which finds it to be a promising alternative to the popular KSB method (Kaiser et al. 1995). Cluster masses were computed using the McADAM software (Marshall 2006) which performs a two-dimensional fit of the individual galaxy shape information of the ‘‘background’’ galaxy catalog. We were thus able to determine: 1) M_{200} derived from fitting NFW profiles (note that only weak constraints could be placed on the concentration parameter, which is generally degenerate without any additional strong lensing constraints); 2) the velocity dispersion σ_v derived from fitting SIS profiles. Although the details of the mass profiles are not well constrained by the weak-lensing analysis, in particular close to the center, the total mass is robust with respect to variations in the concentration parameter of the NFW profile.

We believe that a number of limitations are still affecting our lensing mass estimates: 1) we have only limited knowledge of the redshift distribution of the galaxies used to measured the

shear signal – this may plague the measurement of the shear signal towards the cluster center, although the narrow redshift range of the sample ($\Delta z/z \sim 10\%$) and the homogeneity of the weak lensing data make a direct comparison between the different clusters possible; 2) we could recover the shear signal at best to the 20% level due to a relatively small usable number density of background galaxies (about 10 galaxies per square arc-minute after taking into account a color selection) and a probably not perfect PSF correction; 3) our lensing mass determination assumes circular symmetry which may in some cases be a poor representation of the cluster morphology. Fortunately, thanks to the large spatial extent of the weak-lensing detection the mass-sheet degeneracy in our mass measurements is minimized.

As for the total masses M_{200} of the clusters in our sample, we investigated the relations between mass, X-ray and optical observables. Unlike most previous attempts at calibrating these relations, we use masses measured directly from their gravitational effects employing methods and data that are completely independent of the X-ray measurements. In particular, the errors in the X-ray observables and in the weak-lensing masses are uncorrelated. We summarize the main conclusions and results of the study:

- The optical M/L ratio presents a strong correlation with the cluster luminosity, with $M/L \propto L^{0.80 \pm 0.24}$. The most massive and luminous clusters thus have the highest M/L ratio. This reflects a change in galaxy formation efficiency in rich clusters.
- There is a strong correlation between mass and X-ray luminosity with $L_X \propto M_{200}^{0.83 \pm 0.11}$. The logarithmic slope is significantly smaller than found in previous attempts to compare both quantities. A better understanding of the behavior of this relation is crucial in view of future large X-ray surveys of clusters for most of which only X-ray luminosities will be available.
- The mass range of our cluster sample is too small to correctly fit a $M - T$ relation so we fix the logarithmic slope to $3/2$ and concentrate on determining the normalization to find $M_{200}/10^{14} M_\odot = 0.473 h_{70}^{-1} (T_X/1\text{keV})^{3/2}$. This normalization is very close to the value predicted from numerical cosmological simulations of cluster formation and evolution as well as the observed normalization from X-ray measurements (Ascasibar et al. 2006; Springel 2005). This good agreement also suggests that evolutionary effects are negligible between $z = 0$ and $z = 0.2$.
- The scatter in the $M - T$ relation is still large and difficult to disentangle from uncertainties in the measured masses introduced by limitations in the current lensing analysis. Analysis of larger samples of clusters with, ideally, better weak-lensing data and comparison with simulated data will be required to conclusively address the impact of the hydrodynamical state of clusters and the reliability of X-ray measurements. It is, however, already clear from this study that our eleven clusters differ significantly in terms of global morphology, dynamical state, mass concentration, and thus possibly merging histories.

In the near future, progress on this kind of analysis may be achieved in different ways. Better constraints on mass profiles and particularly on the concentration c will be discussed in a forthcoming combined analysis of strong- and weak-lensing data where the number and positions of strongly lensed or multiply imaged galaxies unambiguously determines the slope of the mass profile in the cluster cores (Hudelot et al., in preparation). First results have already been obtained in Abell 1689 (Limousin et al. 2007) and Abell 68 (Richard et al. 2007). Analysis of larger samples of clusters with current facilities may provide clues on cluster physics by statistically reducing the scatter in the various scaling relations. However, the final limitation may arise from the intrinsic scatter of the X-ray properties (non-equilibrium processes, cluster mergers which tend to increase both X-ray temperature and luminosity) or the lack of accuracy in our lensing measurements. In conclusion, better lensing measurements will likely be obtained, in the near future, with very deep multi-color imaging using wide field cameras (Subaru/SuprimeCam or CFHT/Megacam) or in the more distant future using a space-based wide field imager such as the SNAP telescope.

Acknowledgements. We are grateful to Sarah Bridle and Phil Marshall for many interactions and helpful discussions, especially regarding IM2SHAPE and LENSENT2, their distribution and their use. The referee Thomas Reiprich helped us improve the paper by a lot of useful comments. We wish to thank CALMIP (*CALcul en Midi-Pyrénées*) for making data-processing resources available during the last quarter of 2002 for this CPU-time and RAM consuming analysis. We also thank the Programme National de Cosmologie of the CNRS for financial support. JPK acknowledges support from CNRS and Caltech. IRS and GPS acknowledge support from the Royal Society.

References

- Abell, G. O., Corwin, H. G., & Olowin, R. P. 1989, *ApJS*, 70, 1
- Allen, S. W., Ettori, S., & Fabian, A. C. 2001, *MNRAS*, 324, 877
- Andersson, K. E. & Madejski, G. M. 2004, *ApJ*, 607, 190
- Ascasibar, Y., Sevilla, R., Yepes, G., Müller, V., & Gottlöber, S. 2006, *MNRAS* submitted, astro-ph/0605720
- Bardeau, S., Kneib, J.-P., Czoske, O., et al. 2005, *A&A*, 434, 433, (Paper I)
- Barker, R., Biddulph, P., Bly, D., et al. 2006, *MNRAS*, 369, L1
- Bartelmann, M. 1996, *A&A*, 313, 697
- Bertin, E. & Arnouts, S. 1996, *A&AS*, 117, 393
- Bonamente, M., Joy, M. K., LaRoque, S. J., et al. 2006, *ApJ*, 647, 25
- Borgani, S., Girardi, M., Carlberg, R. G., Yee, H. K. C., & Ellingson, E. 1999, *ApJ*, 527, 561
- Bower, R. G., Benson, A. J., Malbon, R., et al. 2006, *MNRAS*, 370, 645
- Bridle, S., Gull, S., Bardeau, S., & Kneib, J.-P. 2001, in *Proceedings of the Yale Cosmology Workshop: "The Shapes of Galaxies and their Dark Halos"*, ed. N. P. (World Scientific)
- Broadhurst, T., Benítez, N., Coe, D., et al. 2005a, *ApJ*, 621, 53

- Broadhurst, T., Takada, M., Umetsu, K., et al. 2005b, *ApJ*, 619, L143
- Bruzual, G. & Charlot, S. 2003, *MNRAS*, 344, 1000
- Bullock, J. S., Kolatt, T. S., Sigad, Y., et al. 2001, *MNRAS*, 321, 559
- Carlberg, R. G., Yee, H. K. C., & Ellingson, E. 1997, *ApJ*, 478, 462
- Carlberg, R. G., Yee, H. K. C., Ellingson, E., et al. 1996, *ApJ*, 462, 32
- Clowe, D., Bradač, M., Gonzalez, A. H., et al. 2006, *ApJ*, 648, L109
- Clowe, D., Luppino, G. A., Kaiser, N., Henry, J. P., & Gioia, I. M. 1998, *ApJ*, 497, L61
- Clowe, D. & Schneider, P. 2001, *A&A*, 379, 384
- Clowe, D. & Schneider, P. 2002, *A&A*, 395, 385
- Corless, V. L. & King, L. J. 2007, submitted to *MNRAS*, astro-ph/0611913
- Cuillandre, J.-C., Luppino, G. A., Starr, B. M., & Isani, S. 2000, in *Proc. SPIE Vol. 4008*, p. 1010-1021, *Optical and IR Telescope Instrumentation and Detectors*, Masanori Iye; Alan F. Moorwood; Eds.
- Cypriano, E. S., Sodré, L. J., Kneib, J.-P., & Campusano, L. E. 2004, *ApJ*, 613, 95
- Czoske, O. 2002, PhD thesis, Université Paul Sabatier, Toulouse III, France
- Czoske, O., Moore, B., Kneib, J.-P., & Soucail, G. 2002, *A&A*, 386, 31
- Dahle, H., Kaiser, N., Irgens, R. J., Lilje, P. B., & Maddox, S. J. 2002, *ApJS*, 139, 313
- Ebeling, H., Edge, A. C., Allen, S. W., et al. 2000, *MNRAS*, 318, 333
- Ebeling, H., Edge, A. C., Böhringer, H., et al. 1998, *MNRAS*, 301, 881
- Ebeling, H., Voges, W., Böhringer, H., et al. 1996, *MNRAS*, 281, 799
- Egami, E., Kneib, J.-P., Rieke, G. H., et al. 2005, *ApJ*, 618, L5
- Eke, V. R., Cole, S., & Frenk, C. S. 1996, *MNRAS*, 282, 263
- Ellis, R., Allington-Smith, J., & Smail, I. 1991, *MNRAS*, 249, 184
- Evrard, A. E. & Henry, J. P. 1991, *ApJ*, 383, 95
- Fabian, A. C., Sanders, J. S., Allen, S. W., et al. 2003, *MNRAS*, 344, L43
- Finoguenov, A., Böhringer, H., & Zhang, Y.-Y. 2005, *A&A*, 442, 827
- Gavazzi, R., Mellier, Y., Fort, B., Cuillandre, J.-C., & Dantel-Fort, M. 2004, *A&A*, 422, 407
- Giovannini, G., Feretti, L., Govoni, F., Murgia, M., & Pizzo, R. 2006, *Astronomische Nachrichten*, 327, 563
- Girardi, M., Fadda, D., Escalera, E., et al. 1997, *ApJ*, 490, 56
- Gray, M. E., Ellis, R. S., Refregier, A., et al. 2000, *MNRAS*, 318, 573
- Gray, M. E., Taylor, A. N., Meisenheimer, K., et al. 2002, *ApJ*, 568, 141
- Grego, L., Carlstrom, J. E., Reese, E. D., et al. 2001, *ApJ*, 552, 2
- Halkola, A., Seitz, S., & Pannella, M. 2006, *MNRAS*, 372, 1425
- Hennawi, J. F., Dalal, N., Bode, P., & Ostriker, J. P. 2007, *ApJ*, 654, 714
- Heymans, C., Van Waerbeke, L., Bacon, D., et al. 2006, *MNRAS*, 368, 1323
- Kaiser, N., Squires, G., & Broadhurst, T. 1995, *ApJ*, 449, 460, (KSB)
- Kauffmann, G., Colberg, J. M., Diaferio, A., & White, S. D. M. 1999, *MNRAS*, 303, 188
- King, L. J., Clowe, D. I., & Schneider, P. 2002, *A&A*, 383, 118
- King, L. J. & Corless, V. L. 2007, *MNRAS*, 374, L37
- Kneib, J.-P., Ellis, R. S., Santos, M. R., & Richard, J. 2004, *ApJ*, 607, 697
- Kneib, J.-P., Ellis, R. S., Smail, I., Couch, W. J., & Sharples, R. M. 1996, *ApJ*, 471, 643
- Kneib, J.-P., Hudelot, P., Ellis, R. S., et al. 2003, *ApJ*, 598, 804
- Kravtsov, A. V., Vikhlinin, A., & Nagai, D. 2006, *ApJ*, 650, 128
- Landolt, A. U. 1992, *AJ*, 104, 340
- Lavery, R. J. & Henry, J. P. 1988, *ApJ*, 329, L21
- Le Borgne, J.-F., Mathez, G., Mellier, Y., et al. 1991, *A&AS*, 88, 133
- Limousin, M., Richard, J., Kneib, J. K., et al. 2007, *ApJ* submitted, astro-ph/0612165
- Marinoni, C. & Hudson, M. J. 2002, *ApJ*, 569, 101
- Markevitch, M. & Vikhlinin, A. 2007, to appear in *Physics Reports*, astro-ph/0701821
- Marshall, P. 2006, *MNRAS*, 372, 1289
- Marshall, P. J., Hobson, M. P., Gull, S. F., & Bridle, S. L. 2002, *MNRAS*, 335, 1037
- Maughan, B. 2007, *ApJ* submitted, astro-ph/0703504
- McNamara, B. R., Rafferty, D. A., Brizan, L., et al. 2006, *ApJ* submitted, astro-ph/0604044
- Mercurio, A., Girardi, M., Boschini, W., Merluzzi, P., & Busarello, G. 2003, *A&A*, 397, 431
- Metzler, C. A., White, M., & Loken, C. 2001, *ApJ*, 547, 560
- Mieske, S., Infante, L., Benítez, N., et al. 2004, *AJ*, 128, 1529
- Nagai, D., Vikhlinin, A., & Kravtsov, A. V. 2007, *ApJ*, 655, 98
- Natarajan, P. & Kneib, J.-P. 1997, *MNRAS*, 287, 833
- Navarro, J. F., Frenk, C. S., & White, S. D. M. 1997, *ApJ*, 490, 493
- Ota, N. & Mitsuda, K. 2004, *A&A*, 428, 757
- Parker, L. C., Hudson, M. J., Carlberg, R. G., & Hoekstra, H. 2005, *ApJ*, 634, 806
- Paulin-Henriksson, S., Antonuccio-Delogu, V., Haines, C. P., et al. 2007, *A&A*, 467, 427
- Pedersen, L. & Dahle, H. 2006, astro-ph/0603260, *ApJ* submitted
- Pelló, R., Sanahuja, B., Le Borgne, J.-F., Soucail, G., & Mellier, Y. 1991, *ApJ*, 366, 405
- Pelló, R., Schaerer, D., Richard, J., Le Borgne, J.-F., & Kneib, J.-P. 2004, *A&A*, 416, L35
- Peterson, J. R., Paerels, F. B. S., Kaastra, J. S., et al. 2001, *A&A*, 365, L104
- Pierre, M., Le Borgne, J. F., Soucail, G., & Kneib, J. P. 1996, *A&A*, 311, 413
- Popesso, P., Biviano, A., Böhringer, H., Romaniello, M., & Voges, W. 2005, *A&A*, 433, 431
- Reiprich, T. H. 2006, *A&A*, 453, L39

- Reiprich, T. H. & Böhringer, H. 2002, *ApJ*, 567, 716
- Richard, J., Kneib, J.-P., Julló, E., et al. 2007, submitted, astro-ph/0702705
- Richard, J., Schaerer, D., Pelló, R., Le Borgne, J.-F., & Kneib, J.-P. 2003, *A&A*, 412, L57
- Saha, A., Dolphin, A. E., Thim, F., & Whitmore, B. 2005, *PASP*, 117, 37
- Schlegel, D. J., Finkbeiner, D. P., & Davis, M. 1998, *ApJ*, 500, 525
- Smail, I., Ellis, R. S., Dressler, A., et al. 1997, *ApJ*, 479, 70
- Smith, G. P., Kneib, J., Ebeling, H., Czoske, O., & Smail, I. 2001, *ApJ*, 552, 493
- Smith, G. P., Kneib, J.-P., Smail, I., et al. 2005, *MNRAS*, 359, 417
- Smith, G. P., Sand, D. J., Egami, E., Stern, D., & Eisenhardt, P. R. 2006, *ApJ*, 636, 575
- Springel, V. 2005, *MNRAS*, 364, 1105
- Stetson, P. B. 2000, *PASP*, 112, 925
- Teague, P. F., Carter, D., & Gray, P. M. 1990, *ApJS*, 72, 715
- Treu, T., Ellis, R. S., Kneib, J.-P., et al. 2003, *ApJ*, 591, 53
- Voit, G. M. 2005, *Rev. Mod. Phys.* 77, 207
- Wright, C. O. & Brainerd, T. G. 2000, *ApJ*, 534, 34
- Yee, H. K. C., Ellingson, E., Abraham, R. G., et al. 1996, *ApJS*, 102, 289
- Zhang, Y. Y., Finoguenov, A., Böhringer, H., et al. 2007, *A&A*, 467, 437
- Zwicky, F. 1937, *ApJ*, 86, 217

Appendix A: Shear profiles of the cluster sample

The shear profiles for all clusters are shown in Fig. A.1. They are based on the “red galaxy” catalog and feature statistically independent data points. We also plot the results of the McAdam fits obtained with the two mass profiles discussed in the main body of this paper (SIS and NFW, see Table 5). The shear signal in the central bin is generally similar to or weaker than the signal in the second bin. This is likely due to residual contamination from cluster members or foreground galaxies in the catalogs.

Appendix B: Individual properties of the clusters

B.1. Abell 68

Abell 68 contains a large cD galaxy elongated in the NW-SE direction. About $1'$ to the North-West of the cD is a compact group of about five bright galaxies, which gives the system a bimodal appearance. Many blue arclets can be seen around the cluster center and Smith et al. (2005) provide several redshift identifications for these objects. Most notable is a triple arc located just east of the center of the cD galaxy. Recent integral-field spectroscopic observations revealed very strong Lyman- α emission corresponding to an extended object at $z \approx 2.63$ (Richard et al. 2007). This dedicated spectroscopic survey of all the lensed galaxies in this cluster also provides a catalog of 27 images with spectroscopic identification and redshifts ranging from 0.4 up to 5.4, which considerably improves the

central part of the mass model. The strong-lensing model and the weak-lensing signal appear to be in good agreement in this cluster although they are in disagreement with the previously measured weak lensing mass of Dahle et al. (2002).

B.2. Abell 209

Abell 209 is dominated by a bright cD galaxy that is elongated in the NW-SE direction. There are no obvious giant arc systems, although Dahle et al. (2002) mention an arc candidate embedded in the envelope of the central galaxy. The internal dynamics of the cluster has been studied in detail by Mercurio et al. (2003) who find a high value of the line-of-sight velocity dispersion ($\sigma_{\text{los}} \approx 1400 \text{ km s}^{-1}$). The presence of a velocity gradient along the main extension of the distribution of the cluster galaxies and evidence for substructure and dynamical segregation suggest that we are observing this system in a late merger phase. This interpretation is supported by the recent detection of a radio halo (Giovannini et al. 2006) which implies that this cluster is a dynamically immature merger. An independent weak-lensing analysis of Abell 209 was performed by Paulin-Henriksson et al. (2007) using the same data retrieved from the CFHT archives. They measured a virial mass $M_{200} = 7.7^{+4.3}_{-2.7} \times 10^{14} M_{\odot}$ inside a virial radius $r_{200} = (1.8 \pm 0.3) \text{ Mpc}$, values that are in good agreement with our own measurements although they were obtained with a different weak-lensing pipeline and methodology. They are also compatible with previous estimates (Dahle et al. 2002). Their results also show a strong elongation of the cluster.

B.3. Abell 267

Abell 267 is very similar in appearance to Abell 209. The cluster is dominated by a giant cD galaxy with large ellipticity. There are no giant arcs and no obviously lensed background galaxies (Smith et al. 2005). The weak-lensing signal is the weakest of the sample, making this one of the least massive systems studied here.

B.4. Abell 383

Abell 383 is dominated by a nearly circular cD galaxy and shows a rich and complex system of giant arcs and arclets (Smith et al. 2001; Smith et al. 2005). These arcs were used to reconstruct the central mass distribution of the cluster with high accuracy. With five multiple-image systems identified in the cluster center and three more faint, tentative systems, the mass distribution in the core is tightly constrained. The central slope of the mass profile is surprisingly steep, but is consistent with the excess mass due to the strong cooling core which feeds baryonic mass to the cD galaxy. The weak-lensing signal, on the other hand, does not present the same characteristics, leading us to conclude that this cluster is highly concentrated but not widely extended.

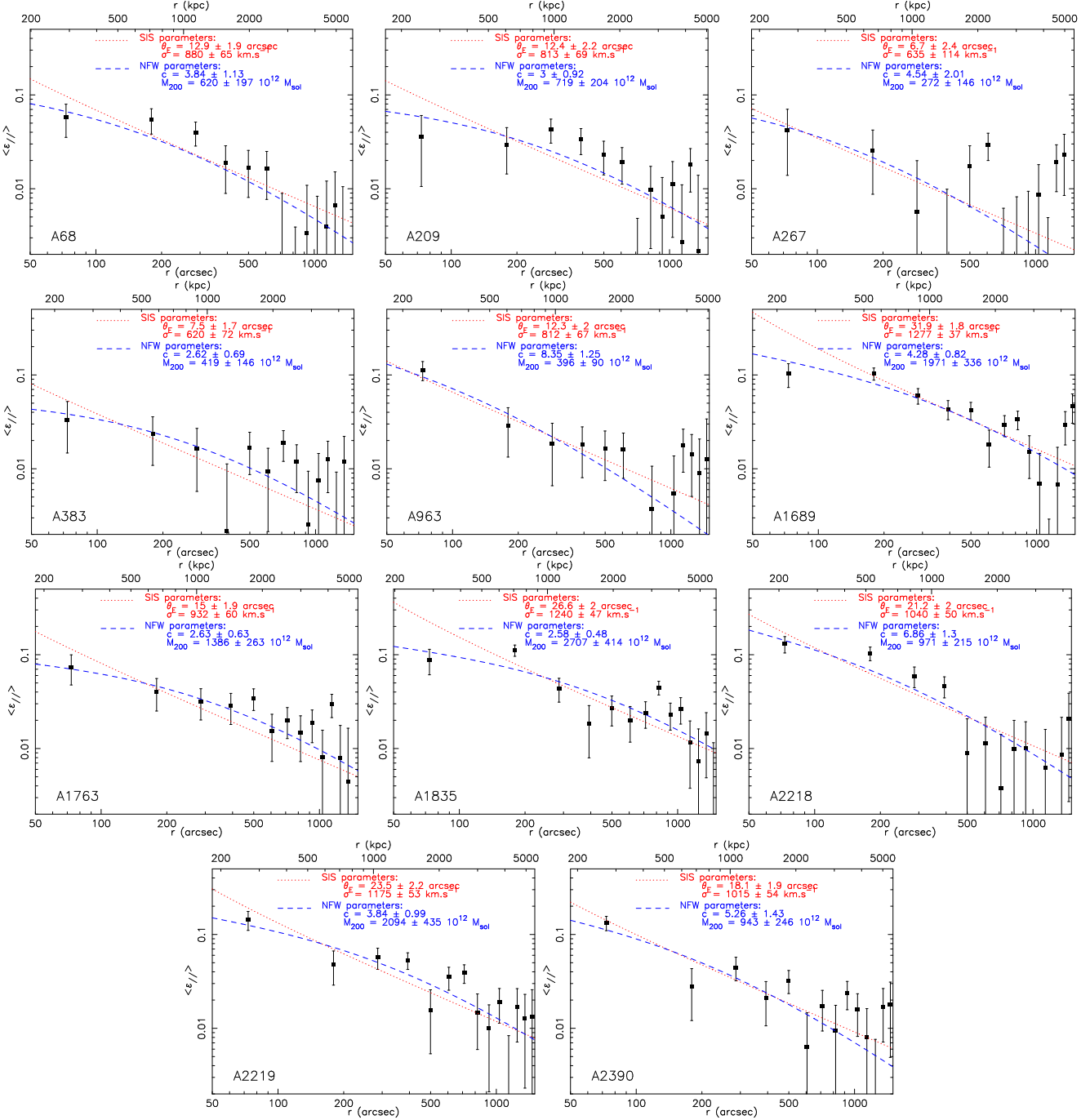


Fig. A.1. Shear profiles of the 11 clusters, using the “red galaxy” catalog. The results of the fits with two different mass profiles (SIS and NFW) using McAdam are shown.

B.5. Abell 963

The center of Abell 963 is dominated by a cD galaxy and contains two giant arcs to the North and the South of the cD, respectively (Lavery & Henry 1988). Ellis et al. (1991) measured a redshift for the northern arc of $z = 0.771$, while the southern arc, of very blue color, has not been identified spectroscopically. From their strong-lensing model, Smith et al. (2005) argue that the southern arc is a group of singly imaged galaxies rather than a multiple-image system. Lavery & Henry (1988) measured a velocity dispersion of 1350^{+200}_{-150} km s $^{-1}$ from

36 cluster members. The weak-lensing signal is remarkably regular and consistent with an NFW profile even at small radii. The spatial distribution of the cluster members is highly circular and characteristic of a well relaxed cluster.

B.6. Abell 1689

Abell 1689 is a well known gravitational lens. It is a very rich and luminous cluster, dominated by a compact group of bright galaxies and a central giant elliptical (gE) galaxy. Deep HST/ACS images reveal a strong over-density of faint com-

pact galaxies in the periphery of this galaxy (Mieske et al. 2004), highlighting its dominance at the center of the cluster. A dynamical study of this cluster was performed by Teague et al. (1990) who found an extremely high velocity dispersion ($\sigma_{\text{los}} = 1989 \text{ km s}^{-1}$) probably arising from a complex merger. Girardi et al. (1997) confirmed this initial assumption with a detailed study of substructure in the cluster and showed that the measured velocity dispersion probably contains a systematic peculiar velocity component caused by an ongoing cluster merger. X-ray properties, such as the low gas mass fraction in this cluster, confirm this interpretation (Andersson & Madejski 2004). Gravitational lensing features have been studied extensively in Abell 1689. Clowe & Schneider (2001) and King et al. (2002) present weak-shear measurements in the cluster which give a global mass profile close to an NFW profile, compatible with the X-ray data, but with a total mass lower than our present measurement by nearly a factor 2. The most spectacular results come from the deep HST/ACS images obtained by Broadhurst et al. (2005a) which display a number of arcs and arclets, making this cluster the most spectacular cluster lens with one of the largest Einstein radii observed in clusters. Halkola et al. (2006) also built a non-parametric strong-lensing mass model and included external weak-lensing constraints to derive a total virial mass, with a value that is 50% higher than our measurement. More recently, an extensive spectroscopic survey of the arcs in this cluster has been conducted (Richard et al. 2007b, in preparation) yielding spectroscopic redshifts for about 2/3 of the 32 multiple image systems identified in the cluster. Using these data, Limousin et al. (2007) constructed an improved mass model combining constraints from both strong and weak lensing. They found a value of 7.6 ± 1.6 for the concentration parameter c , similar to what is expected from numerical simulations (Bullock et al. 2001), a total virial mass $M_{200} = (1.32 \pm 0.2) \times 10^{15} M_{\odot}$, and a virial radius $r_{200} = (2.16 \pm 0.1) Mpc$, in excellent agreement with our results.

B.7. Abell 1763

Abell 1763 has a central cD galaxy but otherwise the cluster center is comparatively ill defined, with “chains” of bright galaxies heading off in at least three directions. There are no obvious gravitational-arc systems in the cluster center. The weak-lensing signal is rather weak even close to the center resulting in a low value for the total mass. The two-dimensional mass reconstruction clearly shows signs of bimodality in this cluster, with the main component centered on the cD galaxy and a second component $4'$ to the west. This second mass structure was not detected by Dahle et al. (2002) because it is beyond their maximum radius of investigation.

B.8. Abell 1835

Abell 1835 is dominated by a giant elliptical galaxy slightly elongated in the North-South direction. The galaxy distribution is regular and the global appearance is that of a well relaxed cluster. A 1835 is the most X-ray luminous cluster in the BCS

catalog (Ebeling et al. 2000) and therefore of the present sample. From the $L_X - T_X$ relation it should also be the hottest cluster; however, its measured X-ray temperature is relatively modest (Table 1) and drops to about 4 keV in the cooling-core region (McNamara et al. 2006). From a lensing point of view, A 1835 is a well known strong-gravitational lens, with many very thin long gravitational arcs seen in the HST/WFPC2 image. Several of them have been identified spectroscopically (Richard et al. 2003; Pelló et al. 2004; Smith et al. 2006), in particular a controversial $z = 10.0$ galaxy. A weak lensing study of this cluster was carried out by Clowe & Schneider (2002) with the Wide Field Imager (WFI) on the ESO/MPG 2.2 m telescope. The isothermal fit agrees well with our work, as does the NFW r_{200} value which gives a total mass of the cluster in very close agreement with our measurement.

B.9. Abell 2218

Abell 2218 is arguably one of the most famous cluster lenses, with an extraordinary number of arcs and arclets in its center. A lens model for this cluster was presented by Kneib et al. (1996) and required a bimodal central mass distribution, with one mass component centered on the cD galaxy and a second one centered on a bright galaxy about $1.5'$ to the south-east of the cD. Girardi et al. (1997) analyzed the distribution of 50 galaxy redshifts in A 2218 and found evidence for two groups of galaxies superimposed along the line of sight, which they identify with the mass clumps modeled by Kneib et al. (1996). Deep HST/ACS images revealed the nature of several strongly lensed galaxies and in particular a $z \sim 7$ galaxy candidate, recently confirmed by Spitzer observations (Kneib et al. 2004; Egami et al. 2005). The weak-lensing signal detected in this cluster is one of the strongest in our sample, and the two-dimensional mass distribution is perfectly matched to the galaxy distribution, with an ellipticity and orientation which reflects the central bimodality of the mass distribution.

B.10. Abell 2219

The optical morphology of Abell 2219 is remarkably similar to that of Abell 2218, with a dominant cD galaxy and a second bright elliptical galaxy at $\sim 1'$ to the South-West. A number of gravitational arcs can be seen, most notably a straight arc between the two brightest cluster galaxies and a very thin and elongated arc to the North-West. The presence of two mass clumps as well as the elongated X-ray distribution indicate a non-relaxed cluster in the process of merging of several substructures. A gravitational depletion signal at near-infrared wavelengths was detected by Gray et al. (2000). The mass deduced from this effect was fitted with a singular isothermal mass distribution with $\sigma \sim 800 \text{ km s}^{-1}$ and is consistent with our measurement. However, our measurement is slightly lower than the one obtained by Dahle et al. (2002). The two-dimensional mass reconstruction reflects the general elongation of the cluster, although this is less significant than in Abell 2218, for example.

B.11. Abell 2390

Abell 2390 is a cD-dominated cluster with several arcs in its center. A chain of fairly bright galaxies extends to the North-West of the cD galaxy. The arcs on this side of the cD are straight (Pelló et al. 1991) and confirm the extension of the underlying mass distribution in this direction. About 3' to the East of the cluster center lies an extended group of galaxies. This cluster has a surprisingly high velocity dispersion (Le Borgne et al. 1991; Yee et al. 1996; Borgani et al. 1999). X-ray observations reveal a strongly elongated gas distribution along the NW-SE axis (Pierre et al. 1996; Allen et al. 2001), consistent with the optical galaxy distribution. Our own two-dimensional mass reconstruction has a similar elongation in the same direction supporting the notion that A 2390 is a non-relaxed cluster, accreting one or two mass clumps along the same axis.